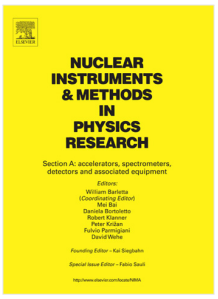
Journal Pre-proof



New measurements of cumulative photofission yields of ^{239}Pu, ^{235}U and ^{238}U with a 17.5 MeV Bremsstrahlung photon beam and progress toward actinide differentiation

M. Delarue, E. Simon, B. Pérot, P.-G. Allinei, N. Estre, D. Eck, E. Payan, I. Espagnon, J. Collot

PII: S0168-9002(22)00600-3
DOI: https://doi.org/10.1016/j.nima.2022.167259
Reference: NIMA 167259

To appear in: *Nuclear Inst. and Methods in Physics Research, A*

Received date : 2 February 2022
Revised date : 31 May 2022
Accepted date : 29 June 2022

Please cite this article as: M. Delarue, E. Simon, B. Pérot et al., New measurements of cumulative photofission yields of ^{239}Pu, ^{235}U and ^{238}U with a 17.5 MeV Bremsstrahlung photon beam and progress toward actinide differentiation, *Nuclear Inst. and Methods in Physics Research, A* (2022), doi: https://doi.org/10.1016/j.nima.2022.167259.

This is a PDF file of an article that has undergone enhancements after acceptance, such as the addition of a cover page and metadata, and formatting for readability, but it is not yet the definitive version of record. This version will undergo additional copyediting, typesetting and review before it is published in its final form, but we are providing this version to give early visibility of the article. Please note that, during the production process, errors may be discovered which could affect the content, and all legal disclaimers that apply to the journal pertain.

© 2022 Published by Elsevier B.V.

Manuscript Revised Final Journal Pre-proof Click here to view linked References

New measurements of cumulative photofission yields of ^{239}Pu, ^{235}U and ^{238}U with a 17.5 MeV Bremsstrahlung photon beam and progress toward actinide differentiation

M. Delarue[1], E. Simon[1*], B. Pérot[1], P.-G. Allinei[1], N. Estre[1], D. Eck[1], E. Payan[1], I. Espagnon[2], J. Collot[3]

[1] CEA, DES, IRESNE, DTN, SMTA, Nuclear Measurement Laboratory, F-13108 St Paul-lez-Durance, France

[2] Université Paris-Saclay, CEA LIST, F-91120 Palaiseau, France

[3] Grenoble INP, LPSC-IN2P3, 38000 Grenoble, France

[*]Corresponding author: eric.simon@cea.fr

Keywords

Photofission, plutonium, uranium, delayed gamma rays, linear accelerator, photofission product yields, MCNP

Abstract

In the frame of a long-term research program on the characterization of large radioactive waste packages by photofission, the Nuclear Measurement Laboratory of CEA IRESNE has measured cumulative yields of ^{239}Pu, ^{235}U and ^{238}U photofission products by using a Bremsstrahlung photon beam produced by a 17.5 MeV linear electron accelerator. A characterization of the energy of the Bremsstrahlung photon beam has been carried out by photon activation analysis with different samples of gold, nickel, uranium, zinc and

Journal Pre-proof

Journal Pre-proof

zirconium. The contribution of neutron fission in the different samples has also been estimated by MCNP simulations in order to assess as precisely as possible the photofission yields. Finally, 26 cumulative photofission product yields are reported for ^{239}Pu, 28 for ^{238}U and 26 for ^{235}U, with half-lives ranging from 14 min to more than 3 days, some of them being not recorded so far in the literature. Among these reported photofission product yields, 18 have been measured for all 3 actinides, which can thus be used for their discrimination. A differentiation criterion based on delayed gamma-ray ratios has been established to determine the most efficient photofission product couples to estimate the enrichment of a ^{235}U/^{238}U mixture or the fissile fraction (^{235}U+^{239}Pu)/actinide mass in a mixture of uranium and plutonium.

1. Introduction

The safety related to the management of radioactive waste (transportation, interim storages and final repositories) is ensured with an accurate non-destructive characterization of their actinide content in relation with the corresponding specifications. Among active non-destructive methods that have been studied to address this characterization in the case of large and dense packages, such as concrete drums [1]-[5], Active Photon Interrogation based on the photofission phenomenon, is the only one that can bring a sufficient signal from the nuclear materials inside the package. Specifically, the detection of delayed gamma radiation emitted by fission products induced by high-energy photons has the potential to assess the actinide mass present in a package, and possibly to distinguish fissile nuclei (that can undergo thermal neutron fission, e.g. ^{235}U and ^{239}Pu) and fertile nuclei (that can absorb a neutron, leading to the formation of a fissile nuclei, e.g. ^{238}U). To that extent, photofission yields of the actinides of interest must be known precisely. Even though nuclear data related to photofission yields of ^{238}U exist, they sometimes present significant discrepancies, even in recent studies [6]-[12]. Photofission yield data are even scarcer for fissile isotopes such as ^{235}U [7][12] and ^{239}Pu [11]-[14], hence the need to perform new measurements.

The potential of analyzing the delayed gamma ray signal following fission to obtain an actinide identification information has already been demonstrated in the past. Hollas *et al.*

[15] and Beddingfield *et al.* [16] have reported the use of delayed gamma-ray ratios for actinide differentiation, respectively for photofission and thermal neutron fission. Further experimental work conducted by Gmar *et al.* [17] pointed out variations of the delayed gamma-ray emissions for uranium samples of different enrichments. Also, Carrel *et al.* [1] brought information about the delayed gamma emission following photofission in mixed samples of ^{235}U and ^{238}U. Besides, the uranium isotopes differentiation in an 870 L waste drum by using delayed gamma-ray ratios has already been investigated experimentally with a mockup package [1] and by using Monte-Carlo simulations in the work of Simon *et al.* [5]. Furthermore, photofission products emitting several gamma rays can be used as attenuation indicators to estimate the depth at which nuclear materials are localized inside the package [18].

In the frame of a long-term research program conducted by the Nuclear Measurement Laboratory of CEA IRESNE Institute in France, this work follows the study recently reported in [19], which provided cumulative photofission yields of ^{235}U and ^{238}U with a 15.8 MeV Bremsstrahlung beam produced by a linear electron accelerator (LINAC) in CINPHONIE casemate of CHICADE nuclear facility [20]. We present here new cumulative photofission yields for ^{239}Pu, and again for ^{235}U and ^{238}U, which are measured with the same setup but with an endpoint electron energy of 17.5 MeV. To this aim, the characterization of the photon beam is first carried out by photon activation analysis with different samples of Au, Ni, U, Zn and Zr. Then we estimate the neutron fission rates in the different samples with MCNP, in view to subtract it from the total fission rate and thus obtain the photofission yields. We also identify photofission products of interest for the differentiation between fissile and fertile actinides.

2. Experimental setup

Experiments were performed by using a Bremsstrahlung photon beam produced by a Saturne LINAC located in the CINPHONIE irradiation cell at CEA Cadarache. In pulse mode, the LINAC accelerates electrons up to 21 MeV. The electrons strike a 5 mm thick tungsten target and a part of their kinetic energy is converted into Bremsstrahlung radiation. The pulse frequency and width are 200 Hz and 4.1 µs, respectively, and the peak current is 100 mA at the target entrance. A 20 cm thick lead collimator allows focusing the beam on

the actinide samples, surrounded by a 20 cm thick shield made of borated polyethylene (BPE) and polyethylene to limit the photoneutron flux reaching the samples, and thus to minimize neutron fissions. A cadmium (Cd) layer of 2 mm was added on the front face to complete the thermal neutron absorption occurring in BPE. A picture of the LINAC configuration and the corresponding simulated model with a materials description are respectively given in Figure 1 and Figure 2. During the experiments, the photon dose rate at 1 m from the tungsten target measured by an ionization chamber was 33 Gy/min.

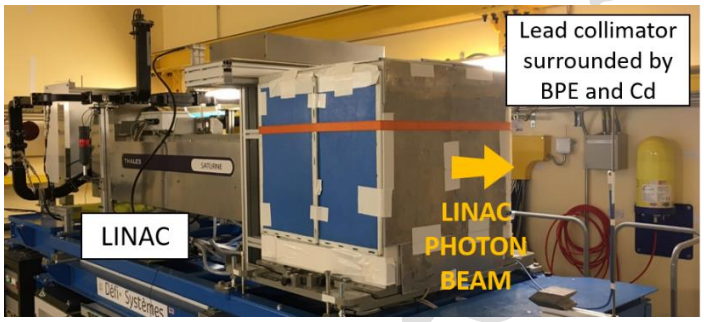


Figure 1: Saturne LINAC with collimator and neutron shielding.

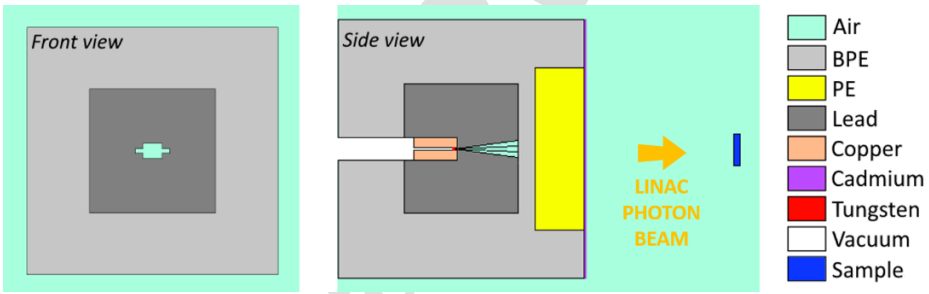


Figure 2: MCNP model of the irradiation configuration (LINAC, lead collimator, neutron shielding and sample).

The photon flux at the output of the collimator aperture being not known precisely, nor the endpoint-energy of the Bremsstrahlung spectrum expected around 16 MeV, a characterization of the photon beam produced by the LINAC is performed using photon activation of reference materials, following the method described in our previous work [19]. The main steps and results of the beam characterization are described in section 3. The pellets irradiated to this aim and positioned in the axis of the LINAC photon beam are described in Table 1. The other pellets in Figure 3 are made of indium (left) and magnesium (right). They were originally designed to be used as neutron activation spectrometers [21] and were irradiated to estimate the photoneutron production in the CINPHONIE irradiation cell (not reported in this paper but used qualitatively in section 4).

Element	Mass (g)	Diameter (mm)	Thickness (mm)	Position on Figure 3
Au	0.045	5	0.05	1
Zn	2.70	19	1.33	2
Ni	10.03	22	3	3

Table 1: Characteristics of the metal pellets irradiated for the photon beam characterization.

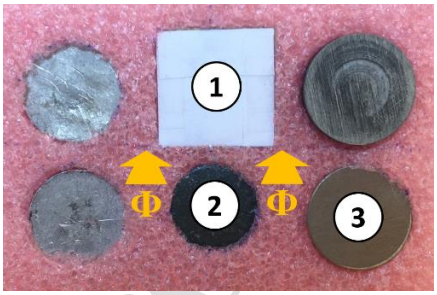


Figure 3: Position of the pellets on their support in view of their common irradiation.

Three actinide samples were irradiated: a sample of Depleted Uranium (DU) which is the same as we used in our previous work [19], a sample of Highly Enriched Uranium (HEU) and a sample of plutonium (Pu). The different samples are described in Table 2.

Table 2: Description of the actinide samples.

Uranium			Plutonium	
Sample	DU	HEU	Sample	Pu
Mass	> 100 g and < 1 kg	> 1 g and < 100 g	Mass	~1 g
^{235}U content	0.3 %	> 90 %	Isotopic composition	^{239}Pu: 83 % ^{240}Pu: 12 %
Composition	Metallic uranium	Metallic uranium core held between Zircaloy sheets		
Dimension	1 cm thickness	< 1 mm thickness	Chemical form	PuO_2 powder mixed with resin
Density	18.96 g.cm^{-3}	Fissile core: 18.96 g.cm^{-3} Zircaloy: 6.56 g.cm^{-3}	Density	1.98 g.cm^{-3}

Since the DU sample is 1 cm thick and composed of metallic uranium of density 18.96 g.cm^{-3}, significant self-attenuation effects occur both for the interrogating photon flux and the delayed gamma rays emitted by photofission products. Therefore, correction factors are applied in order to calculate the photofission product yields (see section 4.2). The plutonium sample is composed of 83 % of ^{239}Pu and 12 % of ^{240}Pu. In this work, we will consider that the sample is made of 95 % of ^{239}Pu since the photofission cross sections for these two isotopes are similar, as seen in Figure 4. It can also be noted that the calculated photofission rates are the same with the real isotopic composition of the plutonium sample and with 100 % of ^{239}Pu. Based on the work of Bernard *et al.* [22] with the GEF code, we can also assume that the cumulative photofission yields of ^{239}Pu and ^{240}Pu are very close, enabling us to consider our plutonium sample as a ^{239}Pu sample without introducing a significant bias in our analyses.

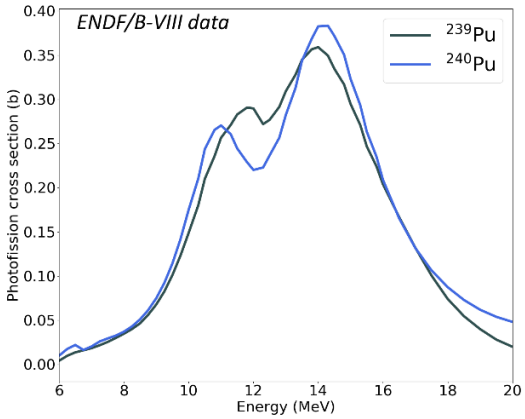


Figure 4: Photofission cross sections of ^{239}Pu and ^{240}Pu [23].

For each actinide sample, a 2 h irradiation with the LINAC is followed by an automatic transfer from the irradiation to the counting position, lasting less than a minute and noted "cooling time" in further activation analysis equations. The samples used to characterize the Bremsstrahlung photon beam were irradiated all together, on the support shown in Figure 3, and transferred to a low-background spectrometer located in another experimental room. Table 3 summarizes the distance and time parameters related to each sample.

Table 3: Experimental distances and timings.

Sample	Denomination	Target-sample distance (cm)	Sample-detector distance (cm)	Irradiation time	Cooling time*	Counting time
Depleted Uranium	DU	102.0	70.0	2 h	19 min	42 h
Highly Enriched Uranium	HEU	102.7	70.7	2 h	42 s	24 h
Plutonium	Pu 1	45.4	13.0	2 h	50 min	24 h
	Pu 2	113.8	24.0	2 h	10 min	21 h
Activation samples (Au, Ni, Zn)	Pellets	88.0	9.5	1 h	390 s	145 h

**See text for the reason of the different cooling times*

Figure 5 shows the layout for every detection configuration. Different screens were added depending on the irradiated samples. For the DU and HEU measurements, only a polyethylene screen was inserted in front of the detector to protect the crystal from fast photoneutron damage during irradiation (it also allows reducing the count rate). A thin cadmium sheet was added in front of the detector to cut the passive emission component of the plutonium sample (59.5 keV due to ^{241}Am). For the "Pu 1" measurement, a lead

shield and a polyethylene screen were used to diminish neutron activation of the detector during irradiation and to reduce the dead-time related to the activation of the surroundings during the measurement (the plutonium sample is inserted between the detector and these shields by a mechanical device). Concerning the metal pellets measurement for the photon beam characterization, the 5 mm Plexiglas screen corresponds to the sample holder.

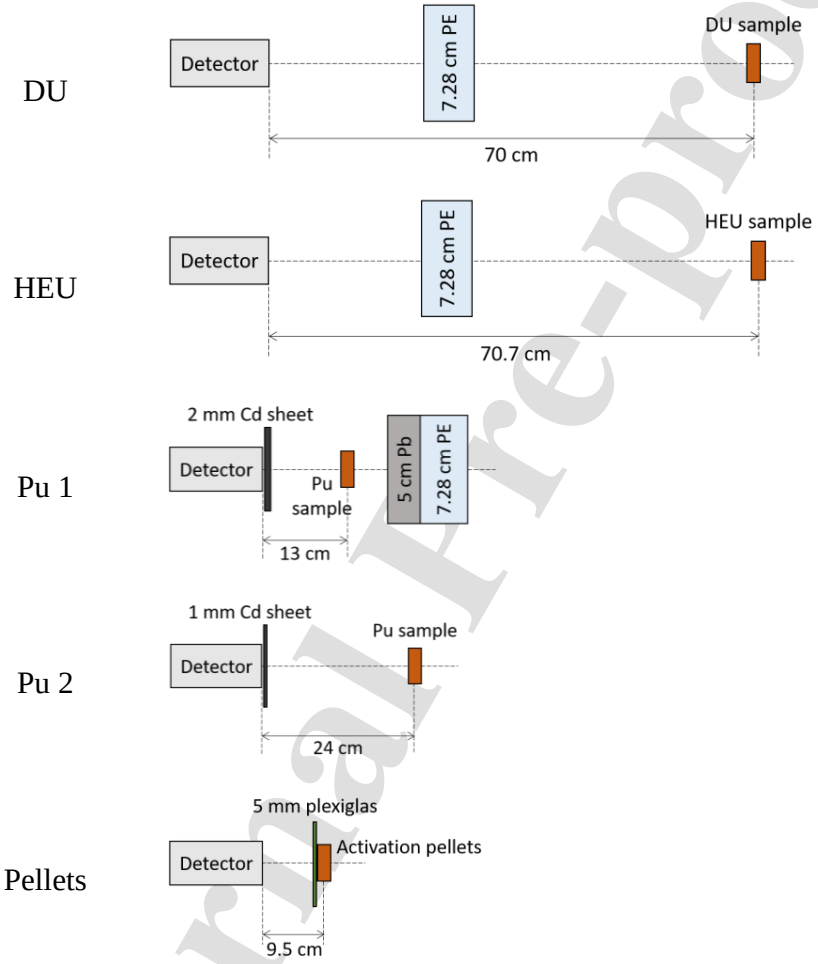


Figure 5: Experimental configuration layout for detection.

The gamma rays of fission and activation products are measured with a 50 % relative efficiency n-type coaxial high-purity germanium detector (HPGe, ORTEC GMX50-83-1-PL) equipped with a transistor-reset preamplifier and coupled to a LYNX Digital Signal Analyzer (CANBERRA) driven by Genie2000 software (MIRION Technologies). The rise time and flat top parameters are respectively set at 2 µs and 0.5 µs following an optimization. The energy resolution is 2.0 keV (FWHM) at the 1332.5 keV gamma line of

Journal Pre-proof

^{60}Co. Although an n-type HPGe crystal is used to limit neutron damage, the detector is shielded by lead and polyethylene, as shown in Figure 6. The analysis of actinide delayed gamma spectra is performed with the MAGIX software developed by CEA LIST, in collaboration with CEA IRESNE Nuclear Measurement Laboratory, to analyze complex gamma- and X-ray spectra measured with HPGe detectors. This automatic software, based on CEA LIST know-how in complex spectrum processing [24][25], performs a complete analysis including energy calibration, identification of radionuclides, peak deconvolution, determination of a relative detection efficiency as a function of energy, activity calculation for each radionuclide if the absolute efficiency is provided by the end-user, and otherwise activity ratios using the relative efficiency. One of its main features is to include iterative steps to identify the radionuclides likely to be associated with each peak of the spectrum, based on the gamma- and X-rays given in JEFF-3.3 database [26] and on a list of possible radionuclides provided by the user.

In order to monitor and correct for the varying dead time during the counting period (due to the rapidly decreasing total count rate), the delayed photofission gamma spectra of the actinide samples were acquired sequentially every 60 s with a spectrum reset. The dead time compensation is a live-time correction, which was assessed to be reliable for dead times below 50 % with the two-source method (^{88}Y + ^{137}Cs as the reference, and ^{152}Eu as the perturbing source responsible of an increasing count rate), prior to LINAC acquisitions. The initial dead times after irradiation were 80 % and 39 %, respectively, for DU and HEU uranium samples. Therefore, the DU sample spectrum was analyzed only after a 19 min cooling time, hence the impossibility to measure short half-life photofission products. As the first measurement of the plutonium sample (Pu 1, cf. Table 3) had an initial dead time of 94 % (dead time fell below 50 % only after 50 min), another irradiation further from the LINAC tungsten target was performed (Pu 2, cf. Table 3), leading to an initial dead time of 61 % that fell below 50 % after 10 min of cooling.

The non-actinide activated metallic samples used for the beam characterization were transferred inside a low-background spectrometer with a 9 % relative efficiency HPGe detector (CANBERRA BEGe 2020) in a lead shield, with inner walls covered by a copper layer to cut lead X-rays. The detector is connected to a digital spectrometer (CANBERRA DSP9660) and the resolution is 1.75 keV (FWHM) at the 1332.5 keV gamma line of ^{60}Co.

The gamma spectrum from the activation pellets was recorded during 6 days after irradiation. Regular resets of the spectrum acquisition were also undertaken to properly correct for dead time. These gamma spectra were analyzed with Genie2000 software (MIRION Technologies).

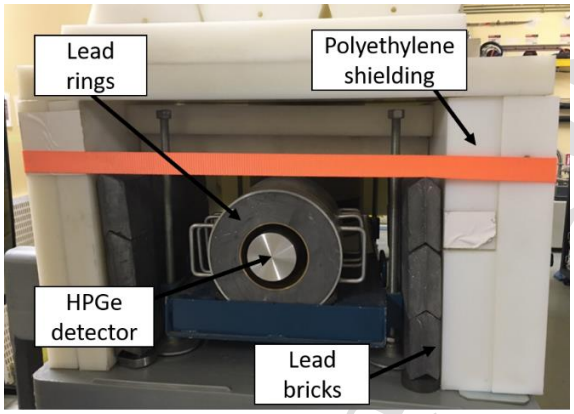


Figure 6: Shielded germanium detector.

3. LINAC photon beam characterization

The photon and neutron activation spectrum of the thin metallic pellets irradiated to characterize the photon beam of the LINAC is given in Figure 7.

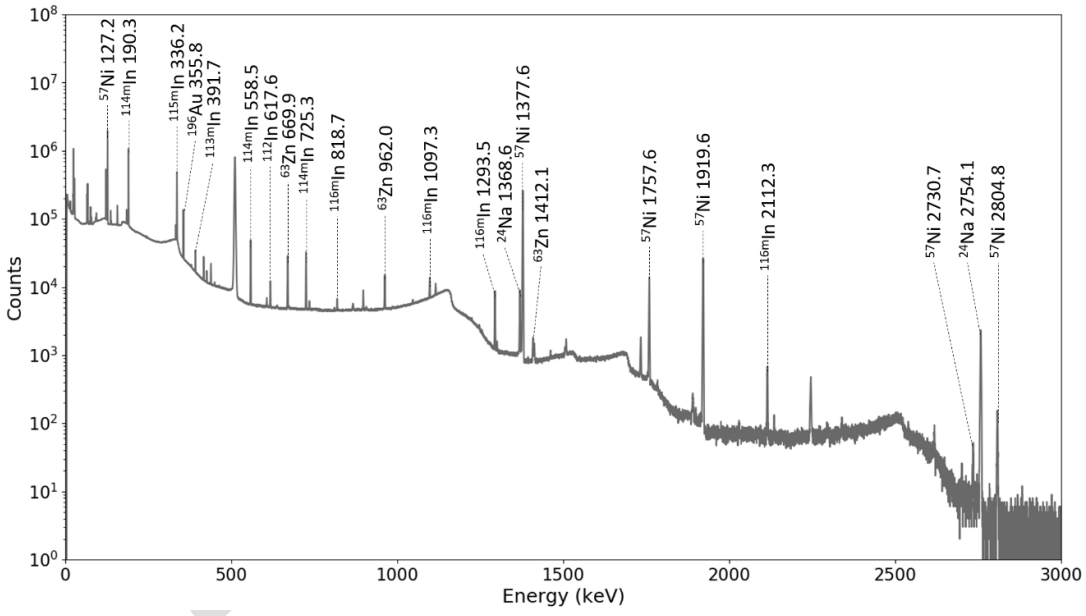


Figure 7: Activation gamma spectrum of the metallic pellets shown in Figure 3.

The detected gamma rays due to (γ,n) activation reactions of gold, zinc and nickel isotopes are reported in Table 4, as well as those of ^{238}U activation in the DU sample and ^{90}Zr activation in the HEU sample (Zircaloy frame, see Table 2). Half-lives and gamma-ray energies are taken from JEFF-3.3 nuclear database [26]. The net areas of the gamma-ray peaks are from the spectra analysis with Genie2000 software. The net area statistical uncertainty is $\sigma(N_{counts}) = \sqrt{N_{counts} + 2B}$, where B is the Compton background under the total absorption peak.

Table 4: Activation gamma rays due to the (γ,n) reaction analyzed to characterize the LINAC photon beam.

Activated isotope	Activation product	Half-life	γ-ray line analyzed (keV)	Net area N_{counts}
^{197}Au	^{196}Au	6.17 days	355.8	549721 ± 741
^{58}Ni	^{57}Ni	35.9 h	1377.6	2411040 ± 1553
^{238}U	^{237}U	6.75 days	208.0	1310540 ± 1145
^{64}Zn	^{63}Zn	38.3 min	669.9	157242 ± 397
^{90}Zr	^{89m}Zr	250.8 s	587.8	37223 ± 193
	^{89}Zr	3.26 days	/	/
	^{89m}Y*	15.7 s	909.0	22248 ± 472

** From the ^{89}Zr and ^{89m}Zr decays*

Since the characteristics of the interrogating photon beam were not known precisely, photon activation of these materials is used to estimate the endpoint-energy of the bremsstrahlung beam and the photon flux, as described in our previous work [19]. The method is based on the differences in the photonuclear cross-sections [27], since each material has a different energy threshold and cross-section for the (γ,n) reaction. Therefore, we are looking for the incident photon flux characteristics that best matches the observed activation of five materials. To this aim, we assume a semi-Gaussian shape of the electron energy distribution, see further Figure 8, of which we are looking for the optimal endpoint-energy and width at half-maximum.

The endpoint-energy was varied from 15 MeV to 18.5 MeV with 0.5 MeV steps, and the width at half-maximum from 0 MeV (mono-energy distribution) to 2 MeV with 0.5 MeV steps. For each of the 40 pairs of parameters, MCNP [28] simulations were performed by impinging electrons of the considered energy distribution on the LINAC tungsten target to produce the Bremsstrahlung photon beam. Then, the number of (γ,n) reactions in each activated sample was numerically evaluated, corresponding to the convolution of the

resulting photon flux on the different materials with their reaction cross-sections. Finally, an experimental photon flux is calculated for each activated isotope (^{197}Au, ^{58}Ni, ^{238}U, ^{64}Zn and ^{90}Zr) by using the net area of the peaks listed in Table 4. As a result, five photon fluxes are obtained for each couple of beam parameters. The most probable electron energy distribution is then identified as the one minimizing the squared differences between these five flux values. In our case, the electron energy distribution with an endpoint-energy of 17.5 MeV and a 0.5 MeV width at half-maximum provides the most consistent photon fluxes for all the materials, as reported in Table 5.

Table 5: Experimental photon fluxes calculated for the five materials with the most probable electron energy distribution.

Activated isotope	$\Phi_{88cm,exp}$ $(photons.cm^{-2}.s^{-1})$
^{197}Au	$(6.82 \pm 0.87) \times 10^{10}$
^{58}Ni	$(7.31 \pm 0.89) \times 10^{10}$
^{238}U	$(6.07 \pm 0.75) \times 10^{10}$
^{64}Zn	$(6.57 \pm 0.84) \times 10^{10}$
^{90}Zr	$(5.97 \pm 0.75) \times 10^{10}$
Mean photon flux $\bar{\phi} = (6.55 \pm 0.94) \times 10^{10}\ photons.cm^{-2}.s^{-1}$	

The uncertainty on the experimental photon flux for each material is calculated as a quadratic combination of the main following sources of uncertainty:

- a relative uncertainty estimated to 10 % on the (γ,n) cross-section of the activated isotopes, according to the EXFOR cross-section library [29]. As an example, the ^{197}Au(γ,n)^{196}Au reaction cross-section uncertainty is about 10 % in the work of Plaisir *et al.* [30];
- a relative uncertainty of 7 % on the detection efficiency to take into account both the detector intrinsic efficiency (less than 5 % thanks to a fine detector model, optimized using reference measurements of standard sources) and the modeling of the experimental set-up (uncertainties on samples and on equipment dimensions, set at 5 % based on our experience of such simulations). Intrinsic and geometric efficiency uncertainties are combined in quadratic sum, leading to a 7 % relative uncertainty on detection efficiency;

- the statistical uncertainty related to MCNP simulation results, which is lower than 2 % for all activation calculations;
- the uncertainties on the radioactive decay constants of the activation products and their gamma-ray intensities, provided by JEFF-3.3 database [26], which are lower than 4 %;
- the uncertainty on the net area of the gamma rays reported in Table 4, which is at most 2.1 %. It is provided by the Genie2000 software and takes into account the uncertainty related to the counting statistics as well as that related to the fitting procedure.

The uncertainty associated to the mean photon flux is here estimated, conservatively, as the quadratic combination of the mean uncertainty of the five calculated photon fluxes (around 12 %) and the standard deviation of the photon fluxes obtained with the five materials:

$$\frac{\sigma_{disribution}}{\bar{\phi}} = \frac{1}{\bar{\phi}}\sqrt{\frac{(\phi_{Au}-\bar{\phi})^2+(\phi_{Ni}-\bar{\phi})^2+(\phi_{U}-\bar{\phi})^2+(\phi_{Zn}-\bar{\phi})^2+(\phi_{Zr}-\bar{\phi})^2}{5}} = 7\ \%;$$

The electron distribution corresponding to the most likely, 17.5 MeV endpoint energy and 0.5 MeV width at half maximum, is shown in Figure 8, and the corresponding Bremsstrahlung photon distribution calculated with MCNP is given in Figure 9.

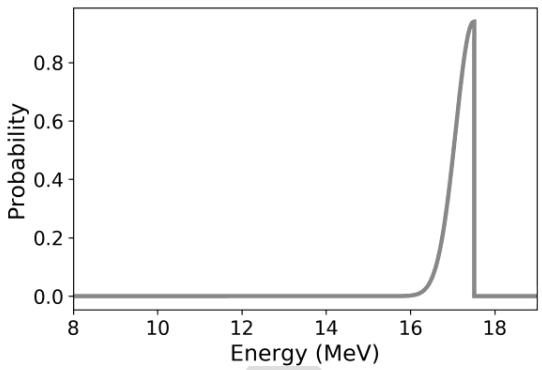


Figure 8: Most probable electron energy distribution (source of MCNP flux and reaction rate calculations).

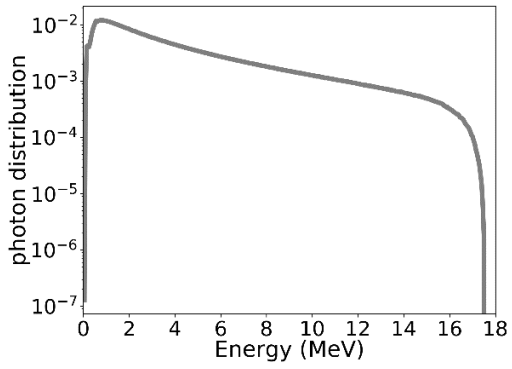


Figure 9: Bremsstrahlung photon energy distribution (normalized) calculated with MCNP and the electron energy distribution of Figure 8.

The mean experimental photon flux of $(6.55 \pm 0.94) \times 10^{10}\ photons.cm^{-2}.s^{-1}$, at the center of the beam and 88 cm away from the tungsten target, will be used to normalize MCNP simulation results that are given per electron impinging on the tungsten target.

4. Comparison of simulated photofission and neutron fission rates

The photofission rate in the samples is defined by (1) for a mixture of n actinides.

$$\tau_p = \frac{\mathrm{N_A}}{\mathcal{M}}\left(\sum_{i=1}^{n} m_i \int_{E_{threshold}}^{E_{max}} \varphi(E)\sigma_{i(\gamma,f)}(E)dE\right) \quad (1)$$

Where:

- τ_p is the photofission rate in s^{-1};
- $\mathrm{N_A}$ is the Avogadro constant, equals to $6.02 \times 10^{23}\ mol^{-1}$;
- $\mathcal{M}$ is the molar mass of the actinide mixture, expressed in $g.mol^{-1}$;
- m_i is the mass of actinide i in the sample, in g;
- $E_{threshold}$ and E_{max} are respectively the threshold energy of the photofission reactions, around 6 MeV, and the Bremsstrahlung endpoint-energy, 17.5 MeV in our case;
- $\varphi(E)$ is the Bremsstrahlung photon flux at the energy E in the sample, in $photons.cm^{-2}.s^{-1}$;
- $\sigma_{i(\gamma,f)}(E)$ is the photofission reaction cross-sections at the energy E for actinide i, in cm^2.

The uncertainty on the photofission rate calculated with MCNP is the quadratic combination of the following uncertainties:

- a 14.3 % relative uncertainty on the Bremsstrahlung photon flux, determined in section 3, $(6.55 \pm 0.94) \times 10^{10}\ photons.cm^{-2}.s^{-1}$ (see Table 5);
- a 0.1 % relative statistical uncertainties on MCNP calculations for the photofission rate in the plutonium, DU and HEU samples;
- a 2 % uncertainty on the photofission cross-section, according to datasets available in the EXFOR library [29];

Finally, using the characteristics of the beam (electron energy distribution and photon flux) and the experimental position of the samples with respect to the tungsten target, the photofission rates in the samples calculated with MCNP are:

$$\tau_{p,\mathrm{Pu\ 1}} = (1.32 \pm 0.19)\,.\,10^{7}\ \mathrm{s}^{-1}$$

$$\tau_{p,\mathrm{Pu\ 2}} = (2.33 \pm 0.34)\,.\,10^{6}\ \mathrm{s}^{-1}$$

$$\tau_{p,DU} = (2.66 \pm 0.38) \,.\, 10^{8}\ s^{-1}$$

$$\tau_{p,HEU} = (3.38 \pm 0.48) \,.\, 10^{7}\ s^{-1}$$

It was shown in our previous work [19] that neutron fissions in the actinides are mainly due to fast neutrons produced in the samples themselves. Indeed, the neutron shielding around the LINAC head (tungsten target and lead collimator), composed of borated polyethylene and cadmium, was proven to be efficient since the presence of thermal neutrons was not observed from neutron activation of the metallic pellets. Indeed, although radiative capture gamma rays of ^{116m}In, due to the ^{115}In(n,γ)^{116m}In activation reaction, highlight the presence of epithermal neutrons with an energy larger than 0.5 MeV (not absorbed by the cadmium foil in front of the LINAC head), thermal neutrons are not detected through the activation of the gold foil. Indeed, we do not observe in the gamma spectrum the 411.8 keV line of ^{198}Au, which was expected from the ^{197}Au(n,γ)^{198}Au reaction, despite a high cross section for thermal neutrons of 100 b (1 b = 10^{-28} m^2) at 0.025 eV according to ENDF/B-VIII.0 library [23].

MCNP simulations were conducted to characterize the origin of the fissions occurring in the samples, i.e. photofission vs. neutron fissions are reported in Table 6, in order to calculate the photofission yields as precisely as possible for the three actinides.

Table 6: Origin of the fissions in the different actinide samples.

Plutonium	
Sample	Pu
Photofissions	98.3 %
Neutron fissions	1.7 %

Uranium		
Sample	DU	HEU
Photofissions of ^{238}U	94.2 %	3.6 %
Photofissions of ^{235}U	-	93.1 %
Neutron fissions of ^{238}U	5.8 %	-
Neutron fissions of ^{235}U	-	3.3 %

In the plutonium sample, the only 1.7 % of neutron fissions will be subtracted to obtain the photofission yields of ^{239}Pu. Besides, given the similarity between the photofission cross sections of ^{239}Pu and ^{240}Pu (cf. Figure 4), we assume that all photofissions occur on ^{239}Pu. Concerning the DU sample with a ^{235}U content of 0.3 %, we consider that all fissions occur on ^{238}U. Among them, 5.8 % are ^{238}U fissions caused by fast neutrons. As a result, the delayed gamma rays measured with the DU sample are used to directly calculate the ^{238}U

photofission products cumulative yields, after subtraction of the neutron fission contribution. In the HEU sample, however, 3.6 % of photofissions occur on ^{238}U and 93.1 % on ^{235}U. Moreover, 3.3 % of fissions are fast neutron fissions on ^{235}U. Therefore, the ^{238}U contribution to photofission and the ^{235}U contribution to neutron fission will be subtracted to calculate the ^{235}U photofission products cumulative yields.

5. Cumulative yields of ^{239}Pu, ^{235}U and ^{238}U photofission products

Figures 10 to 12 show the delayed gamma spectrum of the plutonium sample (denoted as the Pu 1 measurement in Table 3) recorded during 24 h, after a 2 h irradiation with a 17.5 MeV endpoint energy Bremsstrahlung photon beam and a 35 s cooling time. The notations used are PE for Passive Emission, AP for Activation Product and FP for Fission Product. Note that delayed gamma spectra for DU and HEU photofission products have already been presented in our previous work [19].

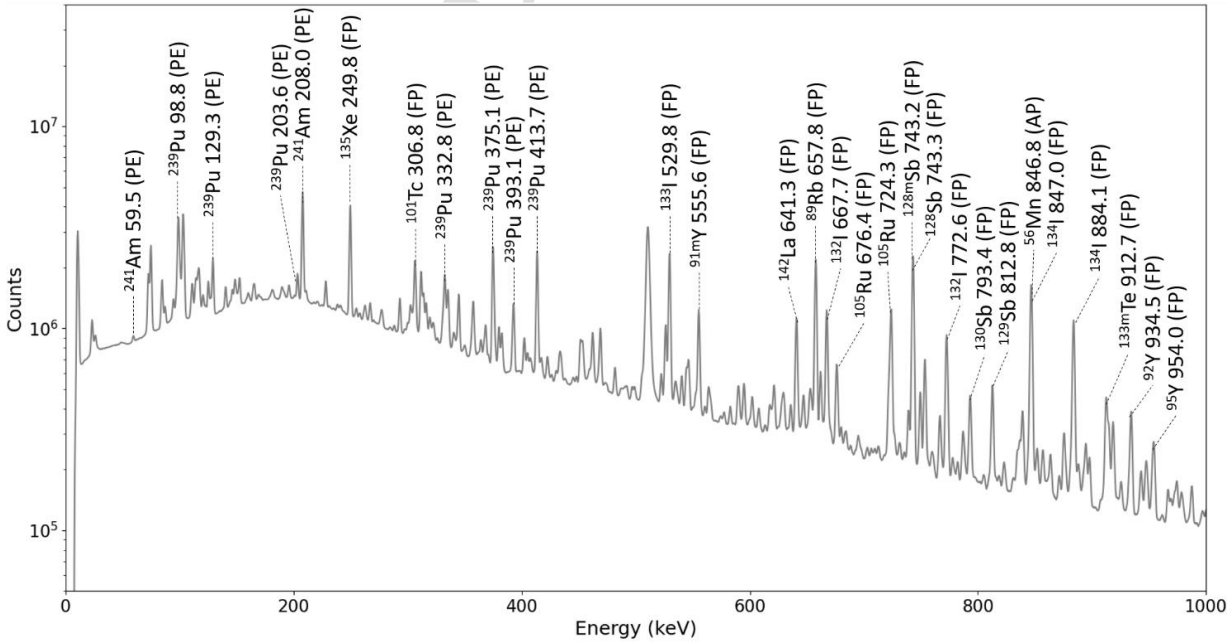


Figure 10: Delayed gamma spectrum of the plutonium sample (0-1000 keV) recorded during 24 h, after a 2 h irradiation and a 35 s cooling time.

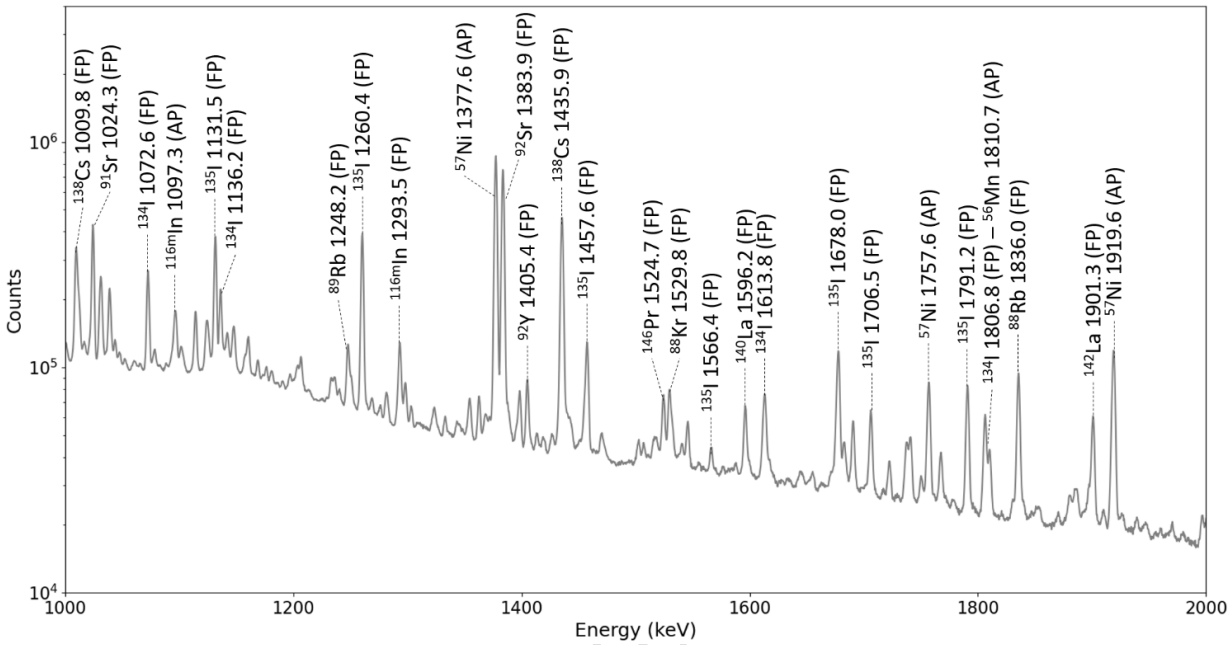


Figure 11: Delayed gamma spectrum of the plutonium sample (1000-2000 keV) recorded during 24 h, after a 2 h irradiation and a 35 s cooling time.

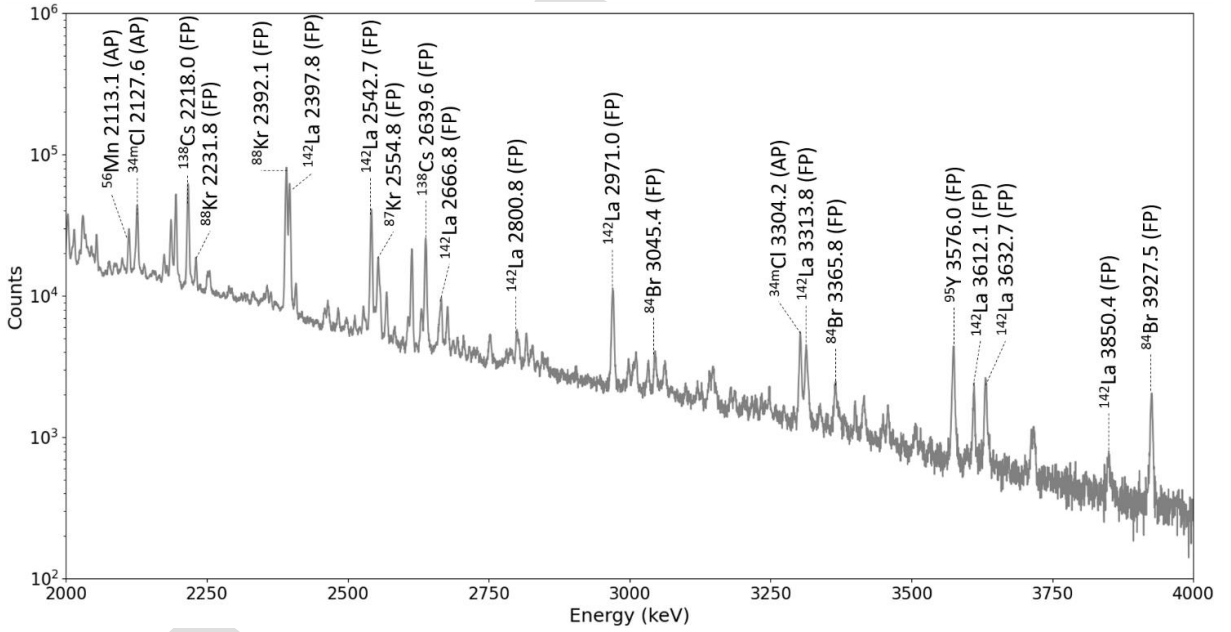


Figure 12: Delayed gamma spectrum of the plutonium sample (2000-4000 keV) recorded during 24 h, after a 2 h irradiation and a 35 s cooling time.

For all actinide samples, the delayed gamma-ray spectra have been recorded by sequences of 60 s during several dozens of hours, which allows a spectrum analysis with different cooling and measurement times to limit some interferences between close-in-energy gamma rays, by exploiting the differences in the radioactive periods of their

emitting isotopes (we can enhance short-lived isotopes by summing the spectra acquired shortly after irradiation, and long-lived ones latter). The spectra analysis is performed with the MAGIX software (see description in Section 2).

Theoretically speaking, the fission products created during irradiation are part of radioactive decay chains and their activities can be calculated by solving Bateman equations [31]. In general, these equations can be simplified by considering only the activation of the photofission product emitting the delayed gamma rays of interest, as below in (2). However, as explained further to introduce (3), it is sometimes needed to consider the direct precursor of the photofission product of interest, which are respectively called the father and daughter nuclides, like in the work of Kahane *et al.* [6] and Carrel *et al.* [7].

For a mixture of two actinides k and l, when the delayed gamma rays are emitted by a nucleus with a much longer half-life than its precursors and the cooling time, the net area $N(E_i)$ of its gamma rays of energy E_i is directly related to cumulative photofission yields $Y_{ck,p}$ and $Y_{cl,p}$ through equation (2):

$$N(E_i) = \frac{I(E_i)\,\varepsilon(E_i)}{\lambda_j}\left(1 - e^{-\lambda_j \cdot t_{irr}}\right)e^{-\lambda_j \cdot t_{cool}}\left(1 - e^{-\lambda_j \cdot t_{count}}\right)\left[\tau_p\left(\eta_{k,p}Y_{ck,p} + \eta_{l,p}Y_{cl,p}\right) + \tau_n\left(\eta_{k,n}Y_{ck,n} + \eta_{l,n}Y_{cl,n}\right)\right] \quad (2)$$

With:

- $I(E_i)$ the gamma-ray intensity taken from JEFF-3.3 database [26];
- $\varepsilon(E_i)$ the absolute detection efficiency taking into account, in addition to the abovementioned intrinsic detector and geometric efficiencies, the interrogating photon flux self-shielding and delayed gamma self-attenuation in the uranium sample, both estimated with MCNP. For example, regarding the self-shielding in the DU sample, the photofission rate is 2.5 times higher on the entrance surface of the sample, with respect to the LINAC photon beam, than on its rear exit surface. Concerning self-attenuation, for instance, less than 60 % of 1 MeV delayed gamma rays emitted in the DU sample manage can escape from it;
- λ_j the radioactive decay constant of the fission product j in s^{-1};
- t_{irr}, t_{cool} and t_{count} respectively the irradiation, cooling and counting time, in s;
- τ_p and τ_n the photofission and neutron fission rates in the sample, in s^{-1};

- $Y_{ck,p}$ and $Y_{cl,p}$ the cumulative photofission yields of photofission product j, respectively for actinides k and l (for example ^{235}U and ^{238}U);
- $Y_{ck,n}$ and $Y_{cl,n}$ the cumulative fast neutron fission product yields of fission product j, respectively for actinides k and l, taken from ENDF/B-VIII.0 database [23];
- $\eta_{k,p}$ and $\eta_{l,p}$ are the fractions of photofissions occurring respectively in actinides k and l, determined via MCNP simulations;
- $\eta_{k,n}$ and $\eta_{l,n}$ are the fractions of neutron fissions occurring respectively in actinides k and l, determined via MCNP simulations.

However, when the photofission product of interest is a daughter nuclide in a decay chain with a father having a similar half-life (for instance ^{134}I and ^{138}Cs, which are respectively the daughters of ^{134}Te and ^{138}Xe, with respective radioactive periods of 41.8 and 33.4 min), net peak areas are given by (3).

$$N(E_i) = I(E_i)\varepsilon(E_i)(\tau_p\left[\eta_{k,p}\left(Y^d_{ik,p}f_d + Y^f_{ck,p}f_f\right) + \eta_{l,p}\left(Y^d_{il,p}f_d + Y^f_{cl,p}f_f\right)\right] \ldots \\ \ldots + \tau_n\left[\eta_{k,n}\left(Y^d_{ik,n}f_d + Y^f_{ck,n}f_f\right) + \eta_{l,n}\left(Y^d_{il,n}f_d + Y^f_{cl,n}f_f\right)\right]) \quad (3)$$

Where:

- $I(E_i)$, $\varepsilon(E_i)$, τ_p, τ_n, $\eta_{k,p}$, $\eta_{l,p}$, $\eta_{k,n}$ and $\eta_{l,n}$ keep the same meaning as in (2);
- $Y^f_{ck,p}$ and $Y^f_{cl,p}$ are the cumulative yields of the father nuclide, respectively for the photofission of actinides k and l;
- $Y^d_{ik,p}$ and $Y^d_{il,p}$ are the independent yields of the daughter nuclide, respectively for the photofission of actinides k and l. The independent yield (in %) of a photofission product corresponds to the number of nuclei created per 100 photofissions of the considered actinide, right after the prompt neutron emission but before the delayed neutron emission. These values will be calculated to determine the cumulative photofission yield of the daughter nuclide, which is the sum of its independent yield with that of its precursor. Note that, as in Kahane *et al.* [6] and Carrel *et al.* [7], we only consider only one precursor, since the precursors of the father nuclide have a relatively short half-life compared to the cooling time of these experiments.

  In this case, we can write $Y^d_{c,p} = Y^d_{i,p} + Y^f_{c,p}$

- $Y^{f}_{ck,n}$ and $Y^{f}_{cl,n}$ are the cumulative yields of the father nuclide, respectively for the neutron fission of actinides k and l. These values are taken from ENDF/B-VIII.0 database [23];
- $Y^{d}_{ik,n}$ and $Y^{d}_{il,n}$ are the independent yields of the daughter nuclide, respectively for the neutron fission of actinides k and l. These values are taken from ENDF/B-VIII.0 database [23];
- The terms f_d and f_f describe the evolution of the respective numbers of daughter and father nuclei over time, and are given by:

$$f_d = \frac{1}{\lambda_d}\left(1 - e^{-\lambda_d.t_{irr}}\right)e^{-\lambda_d.t_{cool}}\left(1 - e^{-\lambda_d.t_{count}}\right)$$

$$f_f = \frac{1}{\lambda_d - \lambda_f}\left[\frac{\lambda_d}{\lambda_f}\left(1 - e^{-\lambda_f.t_{irr}}\right)e^{-\lambda_f.t_{cool}}\left(1 - e^{-\lambda_f.t_{count}}\right) \ldots \right.$$
$$\left. \ldots - \frac{\lambda_f}{\lambda_d}\left(1 - e^{-\lambda_d.t_{irr}}\right)e^{-\lambda_d.t_{cool}}\left(1 - e^{-\lambda_d.t_{count}}\right)\right]$$

With λ_d and λ_f the radioactive decay constants of the daughter and father nuclides (in s^{-1}), respectively, and t_{irr}, t_{cool}, t_{count} the irradiation, cooling and counting times (in s).

Note that when the half-life of the father nuclide is much shorter than that of the daughter nuclide, the cumulative yield of the daughter nuclide can be estimated with (2) by analyzing the delayed gamma spectrum after a cooling time equal to six times the half-life of the father nuclide (corresponding to the decay of 98.5 % of father nuclei). This approach is used in practice for the majority of fission products, the precursors of which having very short half-lives.

For the plutonium sample, the 1.7 % of neutron fissions (see Table 6) are subtracted to obtain the cumulative photofission yields of ^{239}Pu. Concerning the DU sample, with a ^{235}U enrichment of 0.3 %, the measured delayed gamma rays directly lead to the cumulative yields of ^{238}U photofission products, after subtraction of neutron fissions on ^{238}U that represent 5.8 % of total fissions in the sample. For the HEU sample with more than 90 % of ^{235}U, the 3.3 % of neutron fissions are subtracted to obtain the photofission rate, and the 3.6 % of photofissions in ^{238}U are subtracted to calculate the cumulative yields of ^{235}U photofission products. For this purpose, we use the photofission yields obtained in this work for ^{238}U to evaluate the ^{235}U yields. For each case, the fast neutron fission yields

available in ENDF/B-VIII.0 database [23] are used to subtract the neutron fission contribution to the net areas of the gamma rays emitted by the fission products created in the actinide samples.

Finally, 26 and 28 photofission products have been identified in the spectra from their delayed gamma rays, respectively for ^{239}Pu as well as ^{235}U and ^{238}U, and their cumulative photofission yields calculated from (2) or (3). The cumulative photofission yields measured for ^{239}Pu, ^{238}U and ^{235}U are given respectively in Table 7, Table 9 and Table 11. Note that when several delayed gamma rays are measured for a photofission product, we calculate a weighted average of the cumulative yields obtained with all the peaks that are correctly processed by MAGIX software (outliers of the net areas, for instance due to interferences, are discarded). The weighting coefficient for each gamma ray is defined as the inverse of the squared relative uncertainty on the net peak area, as described in (4). Note that the weighted mean does not take into account the accuracy of the emission intensity of the considered gamma rays.

$$\bar{y_c} = \frac{\sum_{i=1}^{N} \frac{y_{c,i}(E_i)}{\left(\frac{\sigma(N(E_i))}{N(E_i)}\right)^2}}{\sum_{i=1}^{N} \frac{1}{\left(\frac{\sigma(N(E_i))}{N(E_i)}\right)^2}} \qquad (4)$$

Where $y_{c,i}(E_i)$ is the cumulative photofission yield calculated with the net peak area $N(E_i)$ of the gamma ray of energy E_i, and $\sigma(N(E_i))$ is the statistical uncertainty calculated by $\sigma(N(E_i)) = \sqrt{N(E_i) + 2B}$, with B the Compton background under this peak.

The uncertainty associated to the average cumulative yield is calculated with a quadratic propagation of the main uncertainties listed below:

- the 14.3 % uncertainty on the photofission rate in the samples (refer to section 4) mainly due to the uncertainty on the interrogating Bremsstrahlung photon flux (section 3). This is the largest part of the overall uncertainty, and it could be reduced in the future by accurately measuring the (γ,n) cross-sections of the activation materials used to characterize the photon beam, since their uncertainties are around 10 % in EXFOR library [29];

- the uncertainty on the absolute detection efficiency of the gamma ray of energy E_i, which is estimated to 7 %;
- the relative statistical uncertainty on the weighted average (5), $\frac{\sigma_{stat}(\overline{y_c})}{\overline{y_c}}$, with $\sigma_{stat}(\overline{y_c}) = \sqrt{\frac{1}{\sum_{i=1}^{N}\left(\frac{N(E_i)}{\sigma(N(E_i))}\right)^2}}$.

The ^{239}Pu cumulative photofission yields measured with the plutonium sample are given in Table 7 and we provide in Table 8 all the details of the delayed gamma-ray analysis: cooling and counting times for each delayed gamma ray, energy and intensity coming from JEFF-3.3 database [26], net peak area with its associated uncertainty, and cumulative yield computed for each line. Our data ("this work") are then compared to the values of photofission products cumulative yields previously published. Note that we report a simple average of the yields when several gamma rays are given in the other publications. The characteristics of the interrogating photon beams are indicated in the first two lines of Table 7. For Bremsstrahlung photon beams, the energy indicated corresponds to the endpoint energy. The nuclides half-lives are from JEFF-3.3 database [26], except for ^{92}Sr because it is not consistent in the different databases, its half-life being taken from Leconte *et al.* [32].

Table 7 : Cumulative yields (number of photofission products per 100 fissions) for the photofission of ^{239}Pu and comparison with published data

Photon beam type ***Energy (MeV)***		Bremsstrahlung 17.5	Bremsstrahlung 28.0	Bremsstrahlung 22.0	Monoenergetic 11.0	Monoenergetic 13.0
Fission product	**$T_{1/2}$**	**This work**	**Kondrat'ko 1981 [13]**	**Wen 2016 [11]**	**Bhike 2017 [14]**	**Krishichayan 2019 [12]**
^{84}Br	31.8 min	1.19 ± 0.19	-	-	-	-
^{87}Kr	1.3 h	2.03 ± 0.32	-	-	-	1.45 ± 0.12
^{88}Kr	2.8 h	2.36 ± 0.36	1.62 ± 0.21	-	-	2.08 ± 0.15
^{89}Rb [(a)]	15.4 min	3.99 ± 0.61	-	3.45 ± 0.43	-	-
^{91}Sr	9.7 h	4.63 ± 0.72	2.89 ± 0.23	-	4.15 ± 0.51	3.91 ± 0.24
^{91m}Y [(a)]	49.7 min	3.19 ± 0.56	-	-	-	-
^{92}Sr	2.6 h	4.73 ± 0.76	-	4.00 ± 0.20	4.21 ± 0.49	4.19 ± 0.66
^{92}Y	3.5 h	5.42 ± 0.93	3.20 ± 0.16	-	-	-
^{93}Y	10.2 h	4.45 ± 0.58	4.02 ± 0.20	-	-	-
^{94}Y [(a)]	18.7 min	7.05 ± 1.13	-	4.60 ±0.32	-	4.71 ± 0.33

^{97}Zr		16.7 h	8.81 ± 1.41	4.63 ± 0.17	-	6.63 ± 0.73	6.78 ± 0.38
^{104}Tc	(a)	18.3 min	6.91 ± 1.12	-	-	-	1.96 ± 0.14
^{105}Ru		4.4 h	6.29 ± 1.01	-	-	-	6.16 ± 0.39
^{105}Rh		34.5 h	7.08 ± 1.11	3.96 ± 0.20	-	-	-
^{128}Sn		59.1 min	1.14 ± 0.18	-	-	-	1.18 ± 0.16
^{128}Sb		9 h	1.14 ± 0.19	-	-	-	-
^{129}Sb		4.4 h	2.60 ± 0.42	-	-	-	2.82 ± 0.15
^{130}Sb		39.5 min	1.64 ± 0.26	-	1.25 ± 0.12	-	1.36 ± 0.11
^{131}Sb	(a)	23 min	2.84 ± 0.45	-	2.10 ± 0.34	-	-
^{134}Te		41.8 min	4.88 ± 0.78	-	11.6 ± 0.81	-	-
^{134}I		52.5 min	7.02 ± 1.16	-	5.90 ± 0.15	7.39 ± 0.89	-
^{135}I		6.6 h	5.67 ± 0.94	-	-	-	-
^{138}Cs		33.4 min	8.24 ± 1.33	-	5.50 ± 0.29	6.18 ± 0.75	6.45 ± 0.37
^{141}Ba	(a)	18.3 min	7.28 ± 1.20	-	-	-	4.22 ± 0.31
^{142}La		1.5 h	6.27 ± 1.00	-	4.90 ± 0.29	-	5.87 ± 0.31
^{143}Ce		1.4 d	4.48 ± 0.76	3.26 ± 0.13	-	4.41 ± 0.51	3.88 ± 0.20

(a)Results obtained with the measurement referred to as Pu 2 in Table 3 and Figure 5. The other cumulative photofission yields of ^{239}Pu are obtained with the Pu 1 measurement.

466

467 *Table 8: Detailed data of the delayed gamma-ray analysis for each ^{239}Pu photofission product*

Fission Product	**Cooling time**	**Counting time**	**Gamma-ray energy (keV)**	**Relative intensity (%)**	**Net peak area (counts)**	**Photofission cumulative yield (%)**
^{84}Br	50.1 min	2.3 h	1897.60	14.56	24858 ± 312	1.23
			1015.90	6.16	18493 ± 565	1.46
			2484.10	6.66	7682 ± 164	1.01
			3927.50	6.78	5977 ± 79	1.16
			1463.80	1.96	3631 ± 357	1.13
^{87}Kr	50.1 min	6.8 h	402.59	49.60	958383 ± 1801	2.00
			2554.80	9.23	74263 ± 308	2.17
			2558.10	3.92	31501 ± 229	2.17
^{88}Kr	50.1 min	16.2 h	196.30	25.98	547139 ± 2605	2.23
			2392.11	34.60	525449 ± 752	2.31
			834.83	12.97	426400 ± 1122	2.64
			1529.77	10.93	224744 ± 660	2.28
			2195.84	13.18	222652 ± 544	2.40
			2029.84	4.53	80749 ± 413	2.39
			2035.41	3.74	66486 ± 394	2.39
			2231.77	3.39	51489 ± 342	2.19
			1518.39	2.15	44384± 508	2.28
^{89}Rb	9.5 min	1.7 h	1032.00	63.60	30790 ± 352	3.80
			1248.20	45.60	21750 ± 277	4.24
			657.80	11.00	7528 ± 523	4.24
			2570.10	10.18	2629 ± 82	3.81
^{91}Sr	1.8 h	22.9 h	1024.30	33.50	1799550 ± 1512	4.50
			749.80	23.68	1580910 ± 1540	4.86
			652.90	8.04	510024 ± 1294	4.33

			652.30	2.98	189136 ± 1163	4.33
^{91m}Y	9.5 min	20.4 h	555.57	95.00	302322 ± 923	3.19
^{92}Sr	1.8 h	22.9 h	1383.90	93.00	3168600 ± 1831	4.74
			953.30	3.62	148282 ± 809	4.64
			1142.39	2.86	108084 ± 785	4.70
^{92}Y	1.8 h	22.9 h	934.50	13.90	1140370 ± 1291	5.42
^{93}Y	1.8 h	22.9 h	266.90	7.42	406743 ± 2240	3.64
			947.10	2.12	137801 ± 806	5.35
			680.20	0.67	45512 ± 1029	4.79
^{94}Y	9.5 min	1.8 h	918.74	56.00	70359 ± 1167	7.05
^{97}Zr	1.8 h	22.9 h	1147.97	2.62	211786 ± 796	8.81
^{104}Tc	9.5 min	2.1 h	535.10	14.69	22763 ± 609	7.00
			884.40	10.95	12685 ± 394	6.44
			893.10	10.23	13116 ± 394	7.18
			1676.80	7.83	6592 ± 196	7.12
			1612.40	5.79	4632 ± 199	6.59
^{105}Ru	1.8 h	22.9 h	724.30	47.30	3994660 ± 2209	6.30
			469.37	17.55	1727880 ± 2019	6.22
			676.36	15.66	1365110 ± 1557	6.30
			316.44	11.12	1076530 ± 2253	6.06
			393.36	3.78	383858 ± 1781	6.22
			875.85	2.50	211630 ± 895	6.93
			969.44	2.11	164478 ± 813	6.66
^{105}Rh	1.8 h	22.9 h	318.90	19.10	1045508 ± 2234	7.07
			306.10	5.10	285966 ± 2103	7.28
^{128}Sn	50.1 min	5.1 h	482.30	59.00	483730 ± 1472	1.14
^{128}Sb	1.8 h	22.9 h	314.10	61.00	1233351 ± 2298	1.20
			754.00	100.00	1639830 ± 1557	1.18
			636.20	36.00	457603 ± 1144	0.86
			628.70	31.00	415906 ± 2162	0.91
^{129}Sb	1.8 h	22.9 h	812.80	47.60	1586460 ± 1505	2.66
			914.50	20.94	584657 ± 1065	2.36
			760.80	3.33	114663 ± 934	2.66
			772.80	3.05	104078 ± 911	2.66
			876.00	2.86	81428 ± 819	2.36
^{130}Sb	50.1 min	3.1 h	793.40	100.00	549107 ± 1050	1.63
			330.91	78.00	569154 ± 1592	1.72
			839.52	100.00	533861 ± 1023	1.63
			182.33	65.00	204834 ± 1730	1.52
			732.00	22.00	100176 ± 888	1.30
^{131}Sb	9.5 min	2.1 h	943.40	46.20	29222 ± 394	2.78
			933.10	25.87	17640 ± 382	2.98
^{134}Te	50.1 min	3.3 h	277.95	21.30	411731 ± 1685	4.88
			201.24	8.90	123133 ± 1767	4.92
^{134}I	50.1 min	8.6 h	857.29	6.70	432668 ± 1051	7.21
			1613.80	4.31	177159 ± 583	6.50
			1741.49	2.57	107325 ± 487	7.34
^{135}I	1.8 h	22.9 h	1260.41	28.70	1844600 ± 1454	5.87
			1131.51	22.59	1416620 ± 1386	5.40
			1038.76	7.95	552762 ± 1017	5.69
			836.80	6.69	476552 ± 1059	5.27
			1678.03	9.56	497395 ± 781	5.65
			1457.56	8.67	499735 ± 818	5.75
			1791.20	7.72	394075 ± 690	5.80
			1124.00	3.62	227641 ± 847	5.40
			1706.46	4.10	211984 ± 563	5.67
^{138}Cs	50.1 min	4.7 h	1435.86	76.30	1214440 ± 1177	8.32
			1009.78	29.83	568411 ± 991	7.97
			2218.00	15.18	178761 ± 486	8.32
			871.8	5.11	103228 ± 795	7.77

Journal Pre-proof

			2639.59	7.63	77034 ± 304	8.12
^{141}Ba	9.5 min	1.7 h	739.20 625.40	4.83 3.59	6597 ± 467 5681 ± 529	7.07 7.64
^{142}La	50.1 min	9.3 h	641.29 894.90 1901.30 1011.40 1043.70	47.40 8.34 7.16 3.93 2.70	3033430 ± 2131 460260 ± 1040 230758 ± 578 202468 ± 856 135455 ± 805	6.28 6.33 5.99 6.34 6.29
^{143}Ce	1.8 h	22.9 h	293.27 350.62 231.55 880.46	42.80 3.23 2.05 1.03	1816230 ± 2477 144406 ± 1899 59502 ± 2382 34612 ± 787	4.78 4.78 4.08 4.82

Our photofission products cumulative yields data for ^{239}Pu are compared in Figure 13 to already published data.

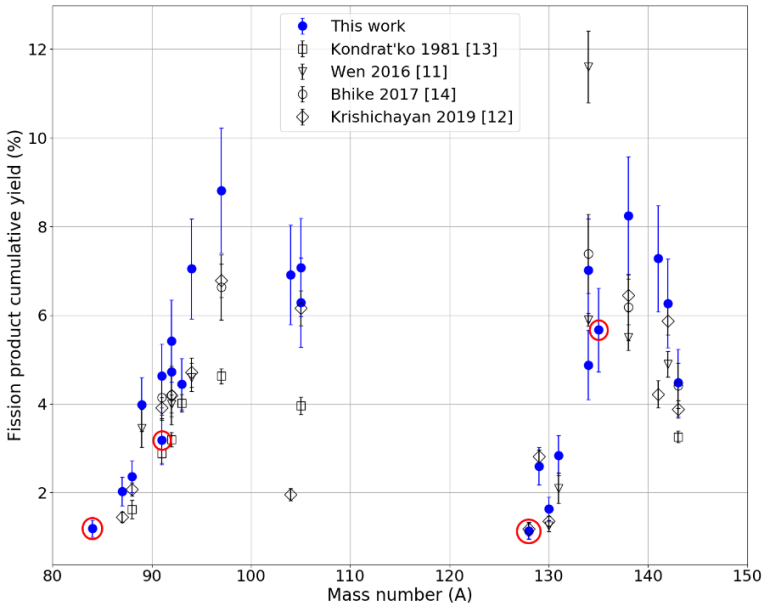


Figure 13: Fission product yields distribution for the photofission of ^{239}Pu and comparison with existing data.

In this work, we provide the cumulative photofission yields of ^{239}Pu fission products ^{84}Br, ^{91m}Y, ^{128}Sb and ^{135}I that were not published before (circled points in Figure 13). We can note that relative yields were recently published by Parlag *et al.* [33] for ^{135}I and ^{91m}Y for a 17.5 MeV Bremsstrahlung endpoint energy, but in this paper, all yields are normalized to that of ^{97}Zr published by Kondrat'ko *et al.* [13] (first dataset published in 1981 concerning the photofission yields of ^{239}Pu), which is significantly lower than other published data and particularly our work, see Table 7. More globally, the photofission yields provided in our work are a little larger but consistent with the other data. We can note a few singular points like the ^{104}Tc yield from Krishichayan *et al.* [12], 1.96 ± 0.14 %,

which is much lower than expected for this mass number. Our work gives 6.91 ± 1.12 % and for comparison, the neutron fission yield is 5.69 % from ENDF/B-VIII.0 database [23]. We can also mention that Kondtrat'ko *et al.* data [13] are globally low and some points also appear as singular, such as the yield of ^{105}Rh, 3.96 ± 0.20 %, compared to our measurement, 7.08 ± 1.11 %, and to the yields of ^{105}Ru with the same atomic number (near 6 %). The yield of ^{134}Te from Wen *et al.* [11] also looks like an outlier with 11.6 ± 0.81 %, compared to our data 4.88 ± 0.78 % and to ^{134}I with this atomic number (near 6-7 %). Except for the singular data mentioned above, the observed discrepancies in the published photofission yields is probably due, for a significant part, to the different experimental configurations (geometry of the samples, energy spectrum and intensity of the interrogating photon beams, photoneutron production, irradiation-cooling-counting times, detectors, etc.) and possibly to data analysis (subtraction of neutron fissions, gamma-ray interferences, decay chain calculations to take into account precursors, etc.). In our case, analyzing several gamma-ray lines for a same photofission product (when possible, for example ^{87}Kr, ^{88}Kr, ^{134}I, ^{135}I, ^{138}Cs, ^{142}La) and observing a good consistency in the different yields associated with each line improves the confidence of the weighted average reported as cumulative yield. It is also important to mention that our results share a common uncertainty of 14 % related to the photon flux assessment. In addition, our plutonium sample is not exclusively made of ^{239}Pu, the photofission yields of the other actinides composing it (^{240}Pu, ^{242}Pu, ^{241}Am) should be investigated with as pure as possible samples in order to evaluate the contribution of each isotope.

The ^{238}U cumulative photofission yields measured with the DU sample are given in Table 9, and the details of the delayed gamma-ray analysis in Table 10.

Table 9: Cumulative yields (number of photofission products per 100 fissions) for the photofission of ^{238}U and comparison with published data

Photon beam type		Bremsstrahlung	Bremsstrahlung	Neutron-capture gamma rays	Bremsstrahlung	Bremsstrahlung	Bremsstrahlung	Bremsstrahlung	Bremsstrahlung	Monoenergetic
Energy (MeV)		17.5	15.8	7.8	16.3	10.0	14.987	8.0	22.0	13.0
Fission Product	**$T_{1/2}$**	**This work**	**Our previous work [19]**	**Kahane 1985 [6]**	**Carrel 2011 [7]**	**Naik 2011 [8]**	**Naik 2013 [9]**	**Naik 2014 [10]**	**Wen 2016 [11]**	**Krishichayan 2019 [12]**
^{84}Br	31.8 min	1.01 ± 0.16	1.37 ± 0.20	-	-	-	0.90 ± 0.06	0.30 ± 0.06	-	2.49 ± 0.19
^{87}Kr	1.3 h	1.90 ± 0.29	1.96 ± 0.31	1.82 ± 0.21	-	1.61 ± 0.20	1.86 ± 0.30	1.11 ± 0.13	1.0 ± 0.06	2.29 ± 0.16
^{88}Kr	2.8 h	2.35 ± 0.38	2.24 ± 0.34	-	2.52 ± 0.23	2.77 ± 0.53	2.58 ± 0.19	2.77 ± 0.38	1.0 ± 0.03	2.92 ± 0.17
^{89}Rb	15.4 min	3.44 ± 0.55	3.50 ± 0.55	2.51 ± 0.40	3.30 ± 0.20	-	3.12 ± 0.16	3.42 ± 0.34	1.4 ± 0.13	-

^{91}Sr	9.7 h	3.93 ± 0.64	3.86 ± 0.60	3.81 ± 0.45	4.53 ± 0.22	3.82 ± 0.17	3.69 ± 0.23	4.75 ± 0.48	-	5.27 ± 0.18
^{92}Sr	2.6 h	4.09 ± 0.66	4.04 ± 0.63	-	4.77 ± 0.22	3.83 ± 0.45	4.26 ± 0.13	4.59 ± 0.47	1.7 ± 0.02	4.82 ± 0.15
^{94}Y	18.7 min	4.87 ± 0.79	4.48 ± 0.77	-	5.06 ± 0.24	-	4.47 ± 0.25	4.25 ± 0.47	-	7.50 ± 0.46
^{97}Zr	16.7 h	5.82 ± 0.94	5.95 ± 0.93	5.89 ± 0.66	-	5.43 ± 0.19	5.78 ± 0.17	6.00 ± 0.64	-	6.20 ± 0.19
^{99}Mo	2.7 d	6.01 ± 0.97	4.65 ± 0.77	-	-	4.84 ± 0.44	5.11 ± 0.15	4.75 ± 0.50	-	6.57 ± 0.22
^{101}Mo	14.6 min	6.56 ± 1.09	5.37 ± 0.86	-	6.78 ± 0.32	-	7.13 ± 0.30	7.56 ± 0.77	-	-
^{104}Tc	18.3 min	3.80 ± 0.63	3.60 ± 0.56	4.13 ± 0.50	-	-	3.65 ± 0.28	4.06 ± 0.42	-	4.44 ± 0.64
^{105}Ru	4.4 h	2.78 ± 0.46	2.76 ± 0.44	2.95 ± 0.45	-	2.57 ± 0.21	2.55 ± 0.06	2.91 ± 0.38	-	4.06 ± 0.20
^{128}Sn	59.1 min	0.58 ± 0.09	0.57 ± 0.09	-	-	-	0.85 ± 0.04	0.21 ± 0.03	-	1.22 ± 0.22
^{128}Sb	9 h	0.22 ± 0.04	0.21 ± 0.03	-	0.16 ± 0.01	-	-	-	-	-
^{129}Sb	4.4 h	1.24 ± 0.20	1.09 ± 0.17	0.54 ± 0.10	1.33 ± 0.06	1.48 ± 0.33	1.35 ± 0.16	0.63 ± 0.06	-	2.59 ± 0.09
^{130}Sb	39.5 min	0.89 ± 0.14	0.79 ± 0.12	-	1.08 ± 0.05	-	-	-	-	1.61 ± 0.11
^{131}Sb	23 min	2.65 ± 0.43	2.51 ± 0.37	-	3.94 ± 0.19	-	4.18 ± 0.18	2.40 ± 0.27	-	5.01 ± 0.33
^{131m}Te	1.3 d	0.86 ± 0.14	0.70 ± 0.10	3.12 ± 0.40	-	-	-	-	-	-
^{132}Te	3.2 d	4.71 ± 0.77	4.71 ± 0.73	2.43 ± 0.50	-	4.84 ± 0.46	5.48 ± 0.14	6.15 ± 0.65	-	5.44 ± 0.25
^{132}I	2.3 h	4.72 ± 0.79	4.87 ± 0.76	3.74 ± 0.46	-	-	-	-	-	-
^{133m}Te	55.4 min	3.19 ± 0.51	3.23 ± 0.44	2.35 ± 0.39	4.43 ± 0.21	-	-	-	3.8 ± 0.42	-
^{134}Te	41.8 min	5.58 ± 0.92	5.29 ± 0.84	6.25 ± 0.89	6.34 ± 0.30	8.27 ± 0.26	7.23 ± 0.33	7.21 ± 0.74	-	7.43 ± 0.51
^{134}I	52.5 min	7.00 ± 1.25	7.30 ± 1.16	6.29 ± 0.94	-	-	8.06 ± 0.34	8.63 ± 0.87	3.1 ± 0.19	-
^{135}I	6.6 h	5.75 ± 0.95	5.85 ± 0.92	5.91 ± 0.68	6.66 ± 0.42	5.88 ± 0.57	5.57 ± 0.12	6.55 ± 0.67	2.6 ± 0.16	6.13 ± 0.29
^{138}Xe	14.1 min	5.59 ± 0.90	3.75 ± 0.59	5.38 ± 0.90	6.60 ± 0.58	-	-	5.91 ± 0.63	1.8 ± 0.41	-
^{138}Cs	33.4 min	5.87 ± 1.11	5.91 ± 0.86	6.10 ± 0.71	-	8.00 ± 0.48	6.84 ± 0.25	6.44 ± 0.68	2.6 ± 0.10	-
^{141}Ba	18.3 min	5.48 ± 0.86	4.75 ± 0.73	-	-	-	4.51 ± 0.23	5.44 ± 0.56	-	-
^{142}La	1.5 h	4.74 ± 0.79	4.89 ± 0.88	3.69 ± 0.43	5.01 ± 0.24	5.26 ± 0.52	4.69 ± 0.20	4.88 ± 0.52	1.7 ± 0.13	5.58 ± 0.18

Table 10: Detailed data of the delayed gamma-ray analysis for each ^{238}U photofission product

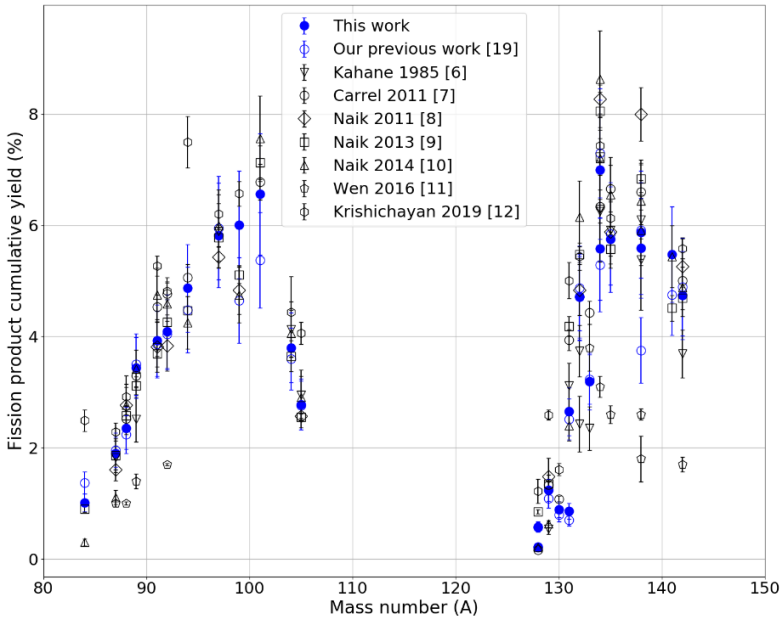
Fission Product	Cooling time	Counting time	Gamma-ray energy (keV)	Relative intensity (%)	Net peak area (counts)	Photofission cumulative yield (%)
^{84}Br	20.0 min	3.2 h	881.60	41.60	72262 ± 695	0.88
			1897.60	14.56	24041 ± 318	0.95
			1015.90	6.16	13767 ± 562	1.13
			802.20	5.99	9578 ± 723	0.82
			2484.10	6.66	10377 ± 173	1.03
			3927.50	6.78	8729 ± 95	1.20
			3365.80	2.87	3461 ± 78	0.99
			3235.30	2.04	2452 ±77	0.95
^{87}Kr	19.0 min	7.6 h	402.59	49.60	250860 ± 1359	1.79
			2554.80	9.23	60419 ± 281	1.97
			2558.10	3.92	25636 ± 211	1.97
			2011.88	2.88	19727 ± 313	1.79
^{88}Kr	19.0 min	16.7 h	2392.11	34.60	400897 ± 659	2.34
			834.83	12.97	191623 ± 938	2.39
			1529.77	10.93	159206 ± 571	2.42
			2029.84	4.53	58502 ± 374	2.39
			2035.41	3.74	48190 ± 358	2.39
			2231.77	3.39	39608 ± 314	2.26

			1518.39	2.15	31391 ± 456	2.42
^{89}Rb	19.0 min	1.7 h	1032.00 1248.20 657.80 2570.10	63.60 45.60 11.00 10.18	149511 ± 623 106176 ± 516 23747 ± 801 17964 ± 177	3.43 3.44 3.47 3.47
^{91}Sr	19.0 min	41.6 h	1024.30 749.80	33.50 23.68	1025360 ± 1223 666694 ± 1258	3.97 3.83
^{92}Sr	19.0 min	16.7 h	1383.90	93.00	2317890 ± 1589	4.09
^{94}Y	19.0 min	1.9 h	918.74 550.9	56.00 4.93	260995 ± 1461 19427 ± 892	4.87 4.94
^{97}Zr	19.0 min	41.6 h	1149.97 1750.24	2.62 1.09	105437 ± 705 39384 ± 399	5.83 5.78
^{99}Mo	19.0 min	41.6 h	739.50	12.12	215280 ± 1085	6.01
^{101}Mo	19.0 min	1.4 h	590.10 1012.47 1532.49	19.21 13.02 6.14	69639 ± 824 52392 ±524 23139 ± 337	6.76 6.49 6.40
^{104}Tc	19.0 min	1.9 h	358.00 535.10 893.10 1596.70 1157.40 2123.80	89.00 14.69 10.23 4.18 2.85 2.23	178773 ± 1124 40712 ± 913 32790 ± 599 14101 ± 332 11038 ± 479 6507 ± 241	3.87 3.57 3.37 3.80 4.10 3.70
^{105}Ru	19.0 min	26.2 h	724.30 676.36 469.37	47.30 15.66 17.55	919049 ± 1370 275906 ± 1169 260961 ± 1454	2.81 2.59 2.76
^{128}Sn	19.0 min	5.6 h	482.30	59.00	93194 ± 1186	0.58
^{128}Sb	1.5 h	40.4 h	754.00	100.00	141414 ± 801	0.22
^{129}Sb	19.0 min	26.2 h	812.80 544.70 966.50 683.50	47.60 18.09 8.14 5.66	403876 ± 1076 141730 ± 1277 66692 ± 746 44137 ± 1051	1.24 1.36 1.16 1.19
^{130}Sb	1.0 h	3.0 h	839.52 793.40 330.91 732.00	100.00 100.00 78.00 22.00	103362 ± 624 109564 ± 652 43614 ± 946 21619 ± 634	0.85 0.92 0.92 0.84
^{131}Sb	19.0 min	1.9 h	943.40 933.10 1207.40 2335.00	46.20 25.87 3.88 1.85	162988 ± 677 90233 ± 626 13656 ± 458 4798 ± 191	2.66 2.63 2.66 2.45
^{131m}Te	19.0 min	41.6 h	852.21	21.40	90922 ± 897	0.86
^{132}Te	40.2 min	41.3 h	228.33	88.12	301254 ± 8404	4.71
^{132}I	19.0 min	41.6 h	667.71	98.7	1128590 ± 1521	4.72
^{133m}Te	19.0 min	7.6 h	912.67 647.51 863.96 914.77	55.27 19.40 15.64 10.94	633754 ± 1055 208071 ± 1112 181664 ± 862 123117 ± 772	3.17 3.25 3.25 3.10
^{134}Te	19.0 min	3.9 h	767.20 565.99 277.95 464.64	29.60 18.60 21.30 5.03	448907 ± 1026 230043 ± 1096 123853 ± 1307 54548 ± 1119	5.67 5.22 5.49 5.32
^{134}I	19.0 min	9.2 h	884.09 1136.16 540.83 1613.80	65.08 9.09 7.66 4.31	2484463 ± 1738 364607 ± 843 252969 ± 1237 159594 ± 543	6.95 7.36 7.49 7.32
^{135}I	19.0 min	38.9 h	1260.41 1131.51 1678.03 1457.56 1038.76 1791.20	28.70 22.59 9.56 8.67 7.95 7.72	1282530 ± 1250 919069 ± 1151 410034 ± 736 388947 ± 768 352406 ± 900 312318 ± 652	5.86 5.22 6.06 6.07 5.72 5.83

Journal Pre-proof

			836.80	6.69	298895 ± 1021	5.95
			1706.46	4.10	175261 ± 549	6.06
			1124.00	3.62	147227 ± 746	5.22
^{138}Xe	19.0 min	1.4 h	1768.26	16.73	49177 ± 340	5.59
^{138}Cs	19.0 min	4.4 h	462.80	30.75	431772 ± 1294	5.83
			871.80	5.11	100812 ± 759	6.13
			408.98	4.66	58254 ± 1179	5.87
^{141}Ba	19.0 min	1.4 h	304.19	25.44	53238 ± 1030	5.28
			343.67	14.44	37741 ± 988	5.60
			739.20	4.83	23791 ± 682	5.78
^{142}La	19.0 min	9.2 h	641.29	47.40	743908 ± 1202	4.93
			2397.80	13.27	156821 ± 415	4.26
			894.90	8.34	134809 ± 672	4.60
			1901.30	7.16	105968 ± 397	4.78
			1011.40	3.93	66289 ± 560	4.76
			2055.20	2.18	31017 ± 274	4.76
			3313.80	0.95	9499 ± 104	4.55

509 Our fission products cumulative yields for ^{238}U are compared in Figure 14 to other existing
510 data.



511

512 *Figure 14: Fission product yields distribution for the photofission of ^{238}U and comparison with existing data.*

513 The values provided for the cumulative photofission yields of ^{238}U through this
514 experimental campaign confirm the results obtained in our previous work [19]. No
515 significant difference of the photofission yields is observed between the 15.8 MeV and
516 17.5 MeV electron endpoint energy, except that of ^{138}Xe for which counting statistics was
517 greatly improved in our new measurement, allowing to refine this yield (and in the same
518 way for ^{101}Mo, to a lesser extent). Wen *et al.* [11] data seem to show a systematic bias and
519 are mostly below the expected values for the different mass numbers of the reported

photofission products. The yield of ^{94}Y from Krishichayan *et al.* [12] also looks like an outlier with 7.50 ± 0.46 %, compared to our data 4.87 ± 0.79 %, which is coherent with all the other datasets displayed.

The ^{235}U cumulative photofission yields measured with the HEU sample are given in Table 11 and the details of gamma analysis in Table 12.

Table 11: Cumulative yields (number of photofission products per 100 fissions) for the photofission of ^{235}U and comparison with published data

Photon beam type		Bremsstrahlung	Bremsstrahlung	Bremsstrahlung	Monoenergetic
Energy (MeV)		17.5	15.8	16.3	13.0
Fission product	**$T_{1/2}$**	**This work**	**Our previous work [19]**	**Carrel 2011 [7]**	**Krishichayan 2019 [12]**
^{84}Br	31.8 min	1.71 ± 0.30	-	-	1.77 ± 0.13
^{87}Kr	1.3 h	3.07 ± 0.53	4.64 ± 0.74	-	3.45 ± 0.28
^{88}Kr	2.8 h	3.59 ± 0.59	5.34 ± 0.84	3.63 ± 0.32	3.87 ± 0.22
^{89}Rb	15.4 min	4.76 ± 0.82	6.89 ± 1.08	4.69 ± 0.28	-
^{91}Sr	9.7 h	4.62 ± 0.82	7.71 ± 1.18	5.37 ± 0.26	6.08 ± 0.26
^{92}Sr	2.6 h	5.17 ± 0.90	7.92 ± 1.24	5.59 ± 0.26	6.52 ± 0.21
^{94}Y	18.7 min	6.03 ± 1.04	-	5.81 ± 0.27	6.84 ± 0.37
^{99}Mo	16.7 h	4.28 ± 0.77	-	-	5.32 ± 0.20
^{101}Mo	14.6 min	5.43 ± 0.96	-	4.19 ± 0.20	-
^{104}Tc	18.3 min	1.99 ± 0.36	1.52 ± 0.24	-	2.37 ± 0.14
^{105}Ru	4.4 h	1.28 ± 0.23	1.86 ± 0.29	-	1.90 ± 0.11
^{128}Sn	59.1 min	0.96 ± 0.16	1.38 ± 0.22	-	1.22 ± 0.16
^{129}Sb	4.4 h	1.67 ± 0.28	2.46 ± 0.36	1.60 ± 0.08	2.47 ± 0.12
^{130}Sb	39.5 min	1.12 ± 0.19	1.49 ± 0.25	1.12 ± 0.05	0.82 ± 0.06
^{131}Sb	23 min	2.03 ± 0.37	3.42 ± 0.53	2.75 ± 0.13	1.59 ± 0.13
^{131m}Te	1.3 d	1.15 ± 0.17	1.98 ± 0.33	-	-
^{132}Te	3.2 d	4.57 ± 0.80	-	-	4.98 ± 0.26
^{132}I	2.3 h	4.89 ± 0.86	-	-	-
^{133m}Te	55.4 min	3.18 ± 0.55	-	4.21 ± 0.20	-
^{134}Te	41.8 min	4.12 ± 0.74	5.33 ± 0.84	3.16 ± 0.15	5.37 ± 0.39
^{134}I	52.5 min	5.00 ± 1.87	7.52 ± 2.22	-	-
^{135}I	6.6 h	4.72 ± 0.85	7.34 ± 1.14	5.06 ± 0.32	4.72 ± 0.21
^{138}Xe	14.1 min	4.35 ± 0.78	7.36 ± 1.18	4.62 ± 0.41	-

^{138}Cs	33.4 min	4.99 ± 1.80	7.79 ± 2.61	-	7.74 ± 0.33
^{141}Ba	18.3 min	5.25 ± 0.88	6.92 ± 1.06	-	4.43 ± 0.27
^{142}La	1.5 h	5.29 ± 0.92	6.39 ± 2.18	5.15 ± 0.24	5.98 ± 0.19

529
530

Table 12: Detailed data of the delayed gamma-ray analysis for each ^{235}U photofission product

Fission Product	Cooling time	Counting time	Gamma-ray energy (keV)	Relative intensity (%)	Net peak area (counts)	Photofission cumulative yield (%)
^{84}Br	19.9 min	2.8 h	881.60 2484.10 3927.50	41.60 6.66 6.78	27836 ± 387 2322 ± 84 1765 ± 42	1.79 1.48 1.56
^{87}Kr	5.8 min	7.5 h	402.59 2554.80 2558.10 2011.88	49.60 9.23 3.92 2.88	178305 ± 914 16155 ± 149 7386 ± 116 5792 ± 182	3.09 2.96 3.20 2.95
^{88}Kr	42 s	17.0 h	196.30 834.83 1529.77 2231.77	25.98 12.97 10.93 3.39	102192 ± 1261 60791 ± 570 34211 ± 325 10623 ± 184	3.46 3.48 3.71 3.55
^{89}Rb	16.9 min	1.8 h	1248.20 2570.10	45.60 10.18	28161 ± 258 4169 ± 85	4.80 4.58
^{91}Sr	5.8 min	23.8 h	1024.30 749.80 925.8	33.50 23.68 3.85	194351 ± 588 146727 ± 674 23247 ± 462	4.68 4.47 4.68
^{92}Sr	42 s	17.0 h	1383.90	93.00	532609 ± 778	5.17
^{94}Y	7.8 min	1.8 h	918.74 1138.9	56.00 5.99	93343 ± 448 9275 ± 271	6.03 6.03
^{99}Mo	9.8 min	23.8 h	739.50 777.92	12.12 4.28	21083 ± 571 7828 ± 530	4.24 4.56
^{101}Mo	42 s	1.4 h	1012.47	13.02	19380 ± 432	5.43
^{104}Tc	5.8 min	2.1 h	358.00 1596.70 3149.20	89.00 4.18 1.16	67074 ± 763 1782 ± 188 334 ± 35	2.00 1.71 1.74
^{105}Ru	46.2 min	23.2 h	724.30 676.36 316.44	47.30 15.66 11.12	85493 ± 557 29663 ± 534 23348 ± 897	1.28 1.31 1.32
^{128}Sn	42 s	5.9 h	482.30 680.50	59.00 15.93	56919 ± 796 16847 ± 590	0.93 1.12
^{129}Sb	1.5 h	22.4 h	812.80 544.70	47.60 18.09	114447 ± 637 49999 ± 766	1.67 1.71
^{130}Sb	1.0 h	2.9 h	793.40 839.52	100.00 100.00	26825 ± 361 26971 ± 346	1.10 1.13
^{131}Sb	5.8 min	2.1 h	943.40 933.10	46.20 25.87	36721 ± 387 18752 ± 366	2.08 1.87
^{131m}Te	42 s	23.9 h	852.21 1125.44	21.40 11.90	14450 ± 527 9653 ± 380	1.00 1.33
^{132}Te	40.1 min	23.3 h	228.33	88.12	129579 ± 1055	4.57
^{132}I	42 s	23.9 h	667.71 522.65 630.19	98.70 15.99 13.32	189532 ± 779 32271 ± 782 26635 ± 693	4.89 4.87 4.93
^{133m}Te	42 s	8.0 h	912.67 647.51 863.96 978.30	55.27 19.40 15.64 4.86	151897 ± 584 61265 ± 665 43916 ± 520 13696 ± 411	3.13 3.23 3.14 3.30
^{134}Te	42 s	4.1 h	767.20	29.60	95959 ± 587	4.12
^{134}I	42 s	9.4 h	884.09 1072.55	65.08 14.93	413068 ± 789 88376 ± 471	5.00 5.00

			595.36	11.10	78034 ± 708	4.87
^{135}I	42 s	23.9 h	1260.41 1131.51 1038.76 1678.03 1457.56	28.70 22.59 7.95 9.56 8.67	176093 ± 518 134550 ± 516 48496 ± 460 52684 ± 322 52650 ± 352	4.80 4.44 4.43 4.92 5.09
^{138}Xe	42 s	1.4 h	1768.26 258.41	16.73 31.50	15536 ± 246 43390 ± 1181	4.34 4.39
^{138}Cs	42 s	4.7 h	1435.86 1009.78 2218.00	76.30 29.38 15.18	271157 ± 573 122123 ± 506 42828 ± 255	4.99 5.03 4.87
^{141}Ba	2.7 min	1.7 h	190.328 304.19 276.95 343.67	46.00 25.44 23.41 14.44	62679 ± 942 54247 ± 828 48450 ± 836 30891 ± 758	4.98 5.37 5.43 5.28
^{142}La	1.1 h	8.7 h	641.29 894.90 1901.30 2187.20 2971.00 2055.20	47.4 8.34 7.16 3.70 3.13 2.18	189460 ± 632 30424 ± 362 18446 ± 188 9598 ± 146 5885 ± 80 5271 ± 136	5.30 5.37 5.17 5.65 4.97 5.04

Our fission products cumulative yields for ^{235}U are compared in Figure 15 to existing published data.

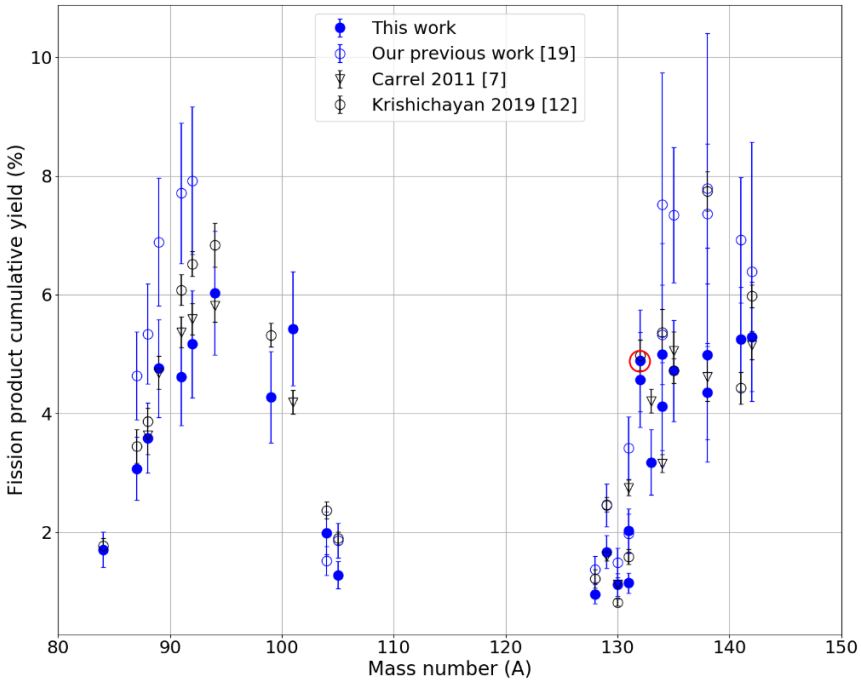


Figure 15: Fission product yields distribution for the photofission of ^{235}U and comparison with existing data.

Contrary to our previous work [19], we were not able to measure the cumulative yields of some short half-life photofission products (like ^{93}Sr or ^{142}Ba, with respective radioactive periods of 7.4 min and 10.6 min) because of the dead time issues mentioned in section 2.

Journal Pre-proof

However, we measured new yields (^{84}Br, ^{91m}Y, ^{99}Mo, ^{101}Mo, ^{132}Te, ^{132}I, ^{133m}Te) that can be compared with existing data. We also provide the ^{235}U cumulative yield for ^{132}I (circled in Figure 15), which was not reported so far in prior publications. For the others, the cumulative yields obtained in this work are consistent with existing data. In particular, we observe a better agreement with Carrel *et al.* [7] than in our previous work. The prior discrepancy was probably due to the poor knowledge of the geometry of the low-mass HEU sample used in the previous experimental campaign [19]. The HEU sample used in this work has a simpler geometry, i.e., a single fissile core instead of several cores separated by Zircaloy spacers.

6. Differentiation of actinide isotopes

As photofission cross sections are of the same order of magnitude for all actinides, the measured delayed gamma-ray signal can provide an estimation of the total nuclear material mass. However, it does not indicate whether it is uranium or plutonium (with very different specific activities, in Bq/g, which is essential for waste management especially for the long-term alpha activity [34]), fissile or fertile isotopes (for criticality safety purpose in waste package transport, interim storage, or final repository). This section deals with the possibility to differentiate actinides using delayed gamma-ray ratios of their photofission products.

When photofission occurs, the formation of two asymmetric fission fragments is the most likely to happen, resulting in a mass distribution curve of the fission products comporting two bumps: one for a heavy nucleus centered around mass number 140, and one for a light nucleus centered around 95. Examples of this theoretical mass distribution for photofission products are given in the work of Bernard *et al.* [22] and reported in Figure 16 for several actinides.

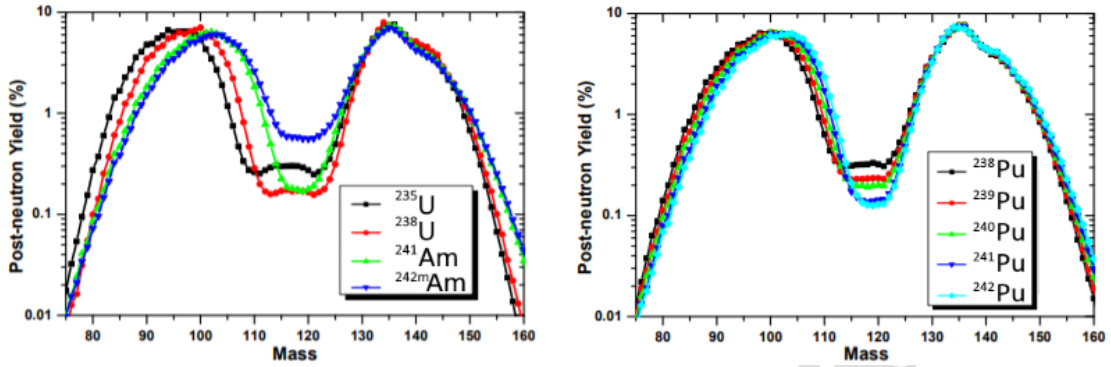


Figure 16: Independent photofission mass yields obtained with the GEF code [35], as reported in ref. [22].

A differentiation information can be obtained between uranium or plutonium isotopes thanks to their different photofission product yields, through the measurement of the relative intensities of specific delayed gamma lines emitted by photofission products having different yields for the different actinides [1][17]. The enrichment, defined as the proportion of the actinide(s) of interest in the mixture, can thus be computed from the ratio of two net areas and from the ratios of the photofission yields of their two emitting photofission products. The objective is to select specific photofission products pairs showing the largest differences, according to the actinide, in their gamma ratios. Some important parameters such as the energy of the gamma rays emitted by the photofission products (related to possible interferences with gamma rays of activation products, matrix attenuation effects, and the level of the Compton continuum under the peaks) and their intensity that determines the achievable counting statistics will also need to be taken into account to identify the most efficient photofission product couples.

For a mixture of ^{235}U and ^{238}U, the net peak area of a delayed gamma-ray line of energy E_i emitted by photofission product j is given by (5):

$$A_j(E_i) = \frac{I(E_i)\varepsilon(E_i)N_A}{\lambda_j} \times \left(1 - e^{-\lambda_j . t_{irr}}\right) \times e^{-\lambda_j . t_{cool}} \times \left(1 - e^{-\lambda_j . t_{count}}\right) \times \ldots \left[Y_{j5}\frac{\alpha m_u}{\mathcal{M}_5}\int_{E_{threshold}}^{E_{max}} \varphi(E)\sigma_5(E)dE + Y_{j8}\frac{(1-\alpha)m_u}{\mathcal{M}_8}\int_{E_{threshold}}^{E_{max}} \varphi(E)\sigma_8(E)dE\right] \quad (5)$$

Where:

- $A_j(E_i)$ is the net peak area of the gamma-ray line of energy E_i emitted by photofission product j;
- $I(E_i)$ is the gamma-ray emission intensity;

- $\varepsilon(E_i)$ is the detection efficiency at energy E_i;
- N_A is the Avogadro constant (in mol^{-1});
- λ_j is the radioactive decay constant of photofission product j (in s^{-1});
- t_{irr}, t_{cool} and t_{count} are respectively the irradiation, cooling and counting times (in s);
- Y_{j5} and Y_{j8} are the cumulative yields of photofission product j for ^{235}U and ^{238}U, respectively;
- m_u is the total uranium mass (in g);
- $\mathcal{M}_5$ and $\mathcal{M}_8$ are respectively the molar masses of ^{235}U and ^{238}U (in g.mol^{-1});
- α is the enrichment, i.e. the proportion of ^{235}U in the uranium mixture;
- $E_{threshold}$ is the threshold energy of the photofission reaction;
- E_{max} is the endpoint energy of the Bremsstrahlung photon beam;
- $\varphi(E)$ is the Bremsstrahlung photon flux at energy E (in cm^{-2}.s^{-1});
- $\sigma_5(E)$ and $\sigma_8(E)$ are the photofission cross sections (in cm²) at energy E for ^{235}U and ^{238}U, respectively.

(5) can be rearranged and written as (6):

$$A_j(E_i) = k_j(E_i) \times m_u \times \left[Y_{j8}(\alpha - 1) - \Sigma\alpha Y_{j5}\right] \quad (6)$$

With:

- $k_j(E_i)$ a constant defined for the sake of simplification, which depends on the photofission product radioactive constant, the gamma-ray intensity and detection efficiency, and the measurement time parameters (irradiation, cooling, counting): $k_j(E_i) = \frac{I(E_i)\varepsilon(E_i)N_A}{\lambda_j} \times (1 - e^{-\lambda_j.t_{irr}}) \times e^{-\lambda_j.t_{cool}} \times (1 - e^{-\lambda_j.t_{count}})$ (in s^{-1}.mol^{-1});
- Σ another simplification constant depending on the actinide mixture, defined as: $\Sigma = \frac{\frac{1}{\mathcal{M}_5}\int_{E_{threshold}}^{E_{max}} \varphi(E)\sigma_5(E)dE}{\frac{1}{\mathcal{M}_8}\int_{E_{threshold}}^{E_{max}} \varphi(E)\sigma_8(E)dE} \approx \frac{\int_{E_{threshold}}^{E_{max}} \varphi(E)\sigma_5(E)dE}{\int_{E_{threshold}}^{E_{max}} \varphi(E)\sigma_8(E)dE}$.

Then, the ratio of the net areas of two delayed gamma rays emitted by two different photofission products is given by (7):

$$R = \frac{k_1}{k_2} \times \frac{Y_{18}(\alpha - 1) - \Sigma\alpha Y_{15}}{Y_{28}(\alpha - 1) - \Sigma\alpha Y_{25}} = \frac{k_1}{k_2} \times R' \quad (7)$$

Where:

- k_1 and k_2 correspond to constants $k_j(E_i)$ described in (6). It is important to mention that we are not limited to ratios of close-in-energy gamma rays. This implies that detection efficiency at both energies has to be estimated and requires a prior localization of actinides, for example with the method described in [18];
- α and Σ have the same meaning as in (5) and (6);
- Y_{18} and Y_{15} are the cumulative yields for the first photofission product for ^{238}U and ^{235}U, respectively;
- Y_{28} and Y_{25} are the cumulative yields for the second photofission product for ^{238}U and ^{235}U, respectively;
- R' is the net area ratio R corrected by the ratio of constants k_1 and k_2 taking into account gamma-ray intensities and detection efficiencies of the two photofission product gamma rays, and irradiation parameters of the two photofission products (exponential terms in (5)).

The efficiency of this differentiation method can be assessed by defining a criterion δ based on the variability of the calculated enrichment compared to the variability of the corrected gamma-ray ratio (8).

$$\delta = \frac{d\alpha}{dR'}\frac{R'}{\alpha} = \frac{\Sigma(Y_{15}Y_{28} - Y_{25}Y_{18})}{\left[\left(\frac{Y_{18}(\alpha - 1) - \Sigma\alpha Y_{15}}{Y_{28}(\alpha - 1) - \Sigma\alpha Y_{25}}\right)(Y_{28} - \Sigma Y_{25}) - Y_{18} + \Sigma Y_{15}\right]^2} \cdot \frac{Y_{18}\frac{\alpha - 1}{\alpha} - \Sigma Y_{15}}{Y_{28}(\alpha - 1) - \Sigma\alpha Y_{25}} \quad (8)$$

By minimizing this criterion over the whole enrichment range, the most appropriate photofission product couples can be identified based on their cumulative photofission product yields reported in previous section for ^{235}U and ^{238}U. The six most efficient photofission product couples for ^{235}U vs. ^{238}U discrimination are thus ^{84}Br/^{105}Ru, ^{105}Ru/^{128}Sn, ^{87}Kr/^{105}Ru, ^{84}Br/^{104}Tc, ^{104}Tc/^{128}Sn and ^{87}Kr/^{104}Tc. The curves representing the ^{235}U enrichment as a function of the R' corrected ratio (deduced from the R measured ratio) are provided in Figure 17, showing that it seems possible to estimate α (or at least the

enrichment range) with the different couples if R' is measured with a reasonably low uncertainty, which will mainly depend on counting statistics uncertainties of the delayed gamma-ray net areas. For instance, a 20 % uncertainty on R' will convert to a relative uncertainty of 65 % on the ^{235}U enrichment, α, for the couple ^{87}Kr/^{105}Ru and a limited enrichment (α=0.2). Besides, a 20 % uncertainty on R' for the couple ^{84}Br/^{105}Ru corresponds to a relative uncertainty of 30 % on α for a higher enrichment (α=0.6). A combination of the results, such as a weighted average of the enrichments obtained with the different couples, will probably be valuable. Further investigation will be conducted to demonstrate the differentiation efficiency of these photofission product couples on real actinide mixtures placed inside a matrix.

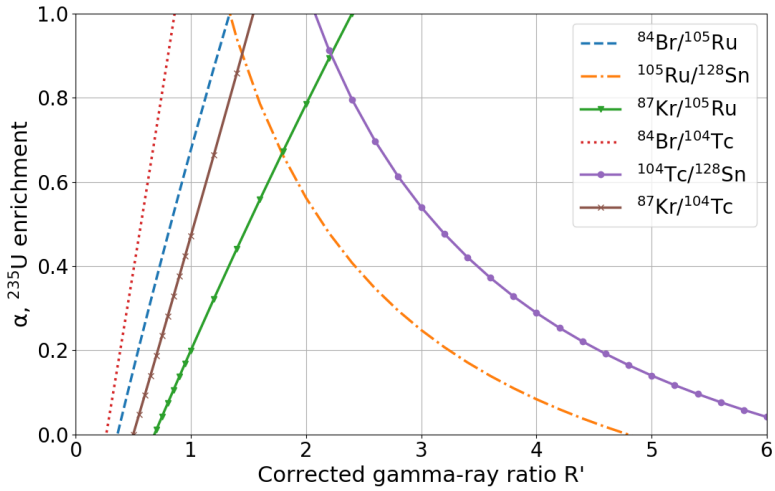


Figure 17: Evolution of ^{235}U enrichment as a function of R' corrected ratio for the 6 most efficient photofission product couples in a ^{235}U/^{238}U mixture.

Beyond a simple uranium mixture only, the photofission product yield values show that a differentiation of the fertile isotope (^{238}U) and the fissile ones (^{235}U and ^{239}Pu considered as a whole), could be achieved since the photofission cross-sections of ^{235}U and ^{239}Pu are similar and that of ^{238}U is way different, as shown in Figure 18. Indeed, there is only a 21% difference between the photofission rate in ^{239}Pu and ^{235}U for the 17.5 MeV endpoint energy Bremsstrahlung spectrum presented in this paper.

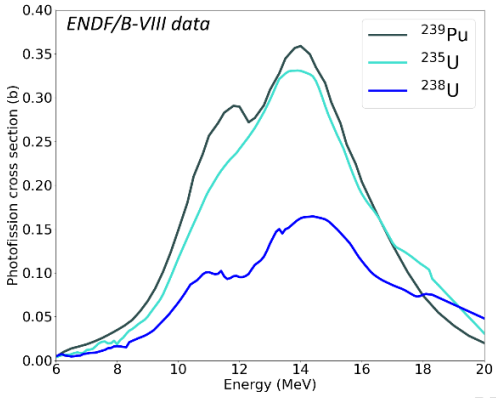


Figure 18: Photofission cross sections of ^{235}U, ^{238}U and ^{239}Pu [23].

The most efficient photofission product couple for that purpose is ^{128}Sn/^{134}Te. The two isotopes share a similar ratio of cumulative yields for ^{235}U $\left(\frac{Y_c(^{128}Sn)}{Y_c(^{134}Te)} = 0.23 \pm 0.06\right)$ and ^{239}Pu $\left(\frac{Y_c(^{128}Sn)}{Y_c(^{134}Te)} = 0.23 \pm 0.05\right)$, and a different ratio for ^{238}U $\left(\frac{Y_c(^{128}Sn)}{Y_c(^{134}Te)} = 0.10 \pm 0.02\right)$. Therefore, ^{235}U and ^{239}Pu can be regarded as a global fissile mass that can be differentiated from ^{238}U mass. The curve representing the fissile actinides proportion as a function of the R' corrected ratio (deduced from the R measured ratio) is provided in Figure 19. Note that the contrast for the differentiation between ^{235}U+^{239}Pu and ^{238}U is lower compared to the differentiation between ^{235}U and ^{238}U in Figure 17.

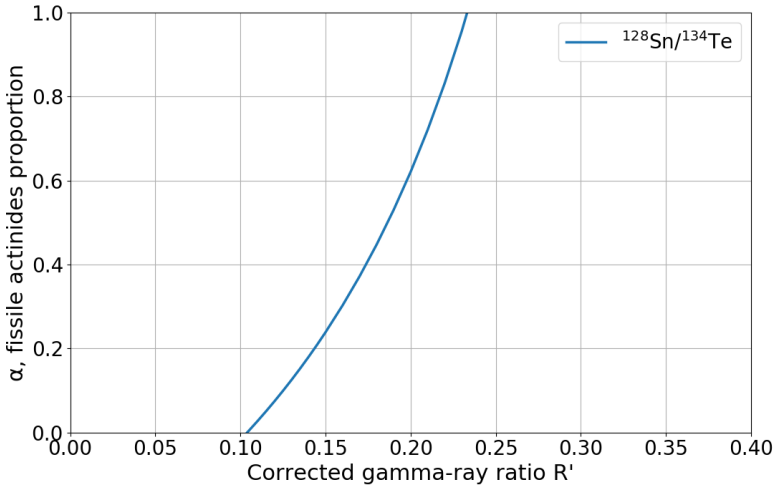


Figure 19: Evolution of the fissile actinides proportion in a ^{235}U/^{239}Pu/^{238}U mixture as a function of R' corrected ratio for the couple ^{128}Sn/^{134}Te

It is worth noting that such a global fissile vs. fertile actinides differentiation based on photofission had not been proposed yet, as the yields of these fission products reported in

Journal Pre-proof

the literature are scarce for ^{235}U or ^{239}Pu, for instance only one measured yield was reported so far concerning ^{128}Sn and ^{134}Te photofission products of ^{239}Pu.

7. Conclusion

New measurements of cumulative photofission yields with a 17.5 MeV endpoint Bremsstrahlung photon beam produced by a SATURNE electron LINAC have been performed in CINPHONIE facility, at CEA Cadarache IRESNE Institute, France. To this aim, a characterization of the Bremsstrahlung photon beam has been first carried out by photon activation analysis with different samples of Au, Ni, U, Zn and Zr. In a former study, we highlighted that most of neutron fissions arise from fast neutrons produced in the actinide sample itself, but not from the photoneutron production in the LINAC components (target, collimator). As a result, the neutron fission rate in the different samples has been numerically estimated with MCNP to subtract it from the total fission rate. Finally, the cumulative production yields of 26 photofission products have been measured for ^{239}Pu and ^{235}U and 28 have been evaluated for ^{238}U. Four of them are not reported in the literature for ^{239}Pu, and one for ^{235}U. Among these available photofission product yields, some show large discrepancies between actinides and thus appear as good candidates for their differentiation based on gamma-ray ratios. To that extent, the six most efficient couples enabling the differentiation between ^{235}U and ^{238}U have been determined. Furthermore, a photofission products couple (^{128}Sn/^{134}Te) has been identified for the differentiation between fissile (^{235}U+^{239}Pu) and fertile (^{238}U) isotopes in a mixture of uranium and plutonium.

Further work will be dedicated to the selection of the most efficient photofission product couples in presence of a waste matrix, causing gamma attenuation effects that depend on actinide localization. To this aim, a new experimental campaign will be carried out to test the differentiation of actinide isotopes inside a concrete matrix, as reported in [18] for actinide localization. One of the main objectives of this long-term R&D program is to assess nuclear materials in heterogeneous technological waste blocked in 870 L cemented drums. Therefore, the quantification of their mass and the differentiation of actinides will be finally tested with an 870 L mock-up drum with uranium and plutonium samples inside.

Journal Pre-proof

Acknowledgements

The authors would like to thank the French National Radioactive Waste Management Agency (ANDRA) contributing for several years to this research and development activity within a cooperation framework under the COV – F32678 DEN4908 – C43R9T5480 contract.

References

[1] F. Carrel, M. Agelou, M. Gmar, F. Lainé, J. Loridon, J.-L. Ma, C. Passard, B. Poumarède, *"Identification and Differentiation of Actinides Inside Nuclear Waste Packages by Measurement of Delayed Gammas"*, IEEE Trans. Nucl. Sci., 57 (5) 2862, (2010).

[2] F. Carrel, M. Agelou, M. Gmar, F. Lainé, *"Detection of high-energy delayed gammas for nuclear waste packages characterization"*, Nuclear Instruments and Methods in Physics Research Section A, vol. 652 (1), 137-139 (2011).

[3] T. Nicol, B. Pérot, C. Carasco, F. Brackx, A. Mariani, C. Passard, E. Mauerhofer, J. Collot, *"Feasibility study of ^{235}U and ^{239}Pu characterization in radioactive waste drums using neutron-induced fission delayed gamma rays"*, Nuclear Instruments and Methods in Physics Research Section A, vol. 832, 85-94 (2016).

[4] R. De Stefano, C. Carasco, B. Pérot, E. Simon, T. Nicol, E. Mauerhofer, *"Feasibility study of fissile mass detection in 870 L radioactive waste drums using delayed gamma rays from neutron-induced fission"*, Journ. Radioanal. Nucl. Chem., vol. 322, 1185-1194 (2019).

[5] E. Simon, F. Jallu, B. Pérot, S. Plumeri, *"Feasibility study of fissile mass quantification by photofission delayed gamma rays in radioactive waste packages using MCNPX"*, Nuclear Instruments and Methods in Physics Research Section A, vol. 840, 28-35, (2016).

[6] S. Kahane, A. Wolf, *"Photofission of ^{238}U with neutron-capture gamma rays"*, Phys. Rev. C, vol. 32, no 6, (1985).

[7] F. Carrel, M. Agelou, M. Gmar, F. Lainé, J. Loridon, J.-L. Ma, C. Passard, (...), B. Poumarède, *"New Experimental Results on the Cumulative Yields From Thermal Fission of ^{235}U and ^{239}Pu and From Photofission of ^{235}U and ^{238}U Induced by Bremsstrahlung"*, IEEE Transactions on Nuclear Science, 58, 2064-2072, (2011).

[8] H. Naik, V. T. Nimje, D. Raj, S. V. Suryanarayana, A. Goswami, S. Singh, S. N. Acharya, K. C. Mittal, S. Ganesan, P. Chandrachoodan, V. K. Manchanda, V. Venugopal, S. Banarjee, *"Mass distribution in the bremsstrahlung-induced fission of ^{232}Th, ^{238}U and ^{240}Pu"*, Nucl. Phys. A 853, 1 (2011).

[9] H. Naik, F. Carrel, G. N. Kim, F. Laine, A. Sari, S. Normand, A. Goswami, *"Mass yield distributions of fission products from photo-fission of ^{238}U induced by 11.5-17.3 MeV bremsstrahlung"*, Eur. Phys. J. A 49, 94 (2013).

[10] H. Naik, B. S. Shivashankar, H. G. Raj Prakash, D. Raj, G. Sanjeev, N. Karunakara, H. M. Somashekarappa, S. Ganesan, G. N. Kim, A. Goswami, *"Measurements of fission yield in 8 MeV bremsstrahlung induced fission of ^{232}Th and $^{238}U"$*, J. Radioanal. Nucl. Chem. 299, 127 (2014).

[11] X. Wen, H. Yang, *"Photofission product yields of ^{238}U and ^{239}Pu with 22-MeV bremsstrahlung"*, Nuclear Instruments and Methods in Physics Research Section A, vol. 821, 34 (2016).

[12] Krishichayan, Megha Bhike, C. R. Howell, A. P. Tonchev, W. Tornow, *"Fission product yields measurements using monoenergetic photon beams"*, Physical Review C 100, 014608 (2019).

Journal Pre-proof

[13] M. Ya. Kondrat'ko, A. V. Mosesov, K. A. Petrzhak, O. A. Teodorovich, *"Yields of photofission of ^{239}Pu"*, Atomnaya Energiya, vol. 50, no 1, 34-36 (1981).

[14] M. Bhike, W. Tornow, Krishichayan, A. P. Tonchev, *"Exploratory study of fission product yield determination from photofission of ^{239}Pu at 11 MeV with monoenergetic photons"*, Physical Review C 95 (2017).

[15] C. L. Hollas, D. A. Close, C. E. Moss, *"Analysis of fissionable material using delayed gamma rays from photofission"*, Nuclear Instruments and Methods in Physics Research Section B, vol. 24-25, Part 1, 503-505 (1987).

[16] D. H. Beddingfield, F. E. Cecil, *"Identification of fissile materials from fission product gamma-ray spectra"*, Nuclear Instruments and Methods in Physics Research Section A, vol. 417, 405-412 (1998).

[17] M. Gmar, J.M. Capdevila, *"Use of delayed gamma spectra for detection of actinides (U,Pu) by photofission"*, Nuclear Instruments and Methods in Physics Research Section A, vol. 422, 841-845 (1999).

[18] M. Delarue, Eric Simon, Bertrand Pérot, Pierre-Guy Allinei, Nicolas Estre, Daniel Eck, Emmanuel Payan, David Tisseur, O. Gueton, Denise Ricard and Johann Collot, "*Localization of nuclear materials in large concrete radioactive waste packages using photofission delayed gamma rays*" EPJ Web of Conferences 253, 08003 (2021)

[19] M. Delarue, E. Simon, B. Pérot, P.G. Allinei, N. Estre, E. Payan, D. Eck, D. Tisseur, I. Espagnon, J. Collot, *"Measurement of cumulative photofission yields of ^{235}U and ^{238}U with a 16 MeV Bremsstrahlung photon beam",* Nuclear Instruments and Methods in Physics Research Section A, vol. 1011 (2021).

[20] B. Pérot, F. Jallu, C. Passard, O. Gueton, P.-G. Allinei, L. Loubet, N. Estre, E. Simon, C. Carasco, C. Roure, L. Boucher, H. Lamotte, J. Comte, M. Bertaux, A. Lyoussi, P. Fichet, F. Carrel, *"The characterization of radioactive waste: a critical*

Journal Pre-proof

review of techniques implemented or under development at CEA, France", EPJ Nuclear Sciences and Technologies 4, 3 (2018).

[21] M. Bricka, V.-D. Nguyen, L. Portheos, *"Le spectromètre neutrons à activation SNAC – Principe – Description – Utilisation"*, CEA R-4226 report (1971).

[22] D. Bernard, O. Sérot, E. Simon, L. Boucher and S. Plumeri, *"A Photofission Delayed γ-ray Spectra Calculation Tool for the Conception of a Nuclear Material Characterization Facility"*, EPJ Web of Conferences 170, 06001 (2018).

[23] D.A. Brown, *et al.*, *"ENDF/B-VIII.0: The 8th Major Release of the Nuclear Reaction Data Library with CIELO-project Cross Sections, New Standards and Thermal Scattering Data"*, Nucl. Data Sheets 148, 1-142 (2018).

[24] A-C. Simon, J-P. Both, I. Espagnon, J. Lefevre, V. Picaud, A. Pluquet, *"A new computer code for the determination of the isotopic composition of actinides by X- and gamma-ray spectrometry and its applications"*, European Nuclear Conference 2005, France (2006).

[25] A-C. Simon, F. Carrel, I. Espagnon, M. Lemercier and A. Pluquet, *"Determination of Actinide Isotopic Composition: Performances of the IGA Code on Plutonium Spectra according to the Experimental Setup",* IEEE Transactions on Nuclear Science, vol 58, no 2 (2011).

[26] A. J. M. Plompen, O. Cabellos, C. De Saint Jean *et al.* The joint evaluated fission and fusion nuclear data library, JEFF-3.3. Eur. Phys. J. A 56 181 (2020).

[27] R. Nath, R.-J. Schulz, *"Determination of high-energy X-ray spectra by photoactivation"*, Medical Physics, vol. 3, no. 3, 133-141 (1975).

[28] Los Alamos National Laboratory, *Mcnp 6™ User's Manual*, Denise B. Pelowitz (2013).

[29] N. Otuka, E. Dupont, V. Semkova, B. Pritychenko, A. I. Blokhin, M. Aikawa, S. Babykina, M. Bossant, G. Chen, S. Dunaeva, R. A. Forrest, T. Fukahori, N. Furutachi, S. Ganesan, Z. Ge, O. O. Gritzay, M. Herman, S. Hlavač, K. Katō, B. Lalremruata, Y. O. Lee, A. Makinaga, K. Matsumoto, M. Mikhaylyukova, G. Pikulina, V. G. Pronyaev, A. Saxena, O. Schwerer, S. P. Simakov, N. Soppera, R. Suzuki, S. Takács, X. Tao, S. Taova, F. Tárkányi, V. V. Varlamov, J. Wang, S. C. Yang, V. Zerkin, Y. Zhuang, *"Towards a More Complete and Accurate Experimental Nuclear Reaction Data Library (EXFOR): International Collaboration Between Nuclear Reaction Data Centres (NRDC)"*, Nucl. Data Sheets 120, 272-276 (2014).

[30] C. Plaisir *et al., "Measurement of the ^{85}Rb(γ, n)^{84m}Rb cross-section in the energy range 10–19 MeV with bremsstrahlung photons"*, Eur. Phys. Journal A 48:68 (2012). (EXFOR G0033.002).

[31] H. Bateman, *"The solution of a system of differential equations occurring in the theory of radioactive transformations"*, Proc. Cambridge Philosophical Society, vol. 15, 423-427 (1910).

[32] P. Leconte, J. P. Hudelot and M. Antony, *"Accurate γ-ray spectrometry measurements of the half-life of ^{92}Sr"*, Applied Radiation and Isotopes, vol. 66, issue 10, 1450-1458 (2008).

[33] O. O. Parlag, V. T. Maslyuk, E. V. Oleynikov, I. V. Pylypchynets, A. I. Lengyel, *"Product yields for the photofission of ^{239}Pu with bremsstrahlung at 17.5 MeV boundary energy"*, Problems of Atomic Science and Technology, vol. 136 (2021).

[34] ANDRA (French Radioactive Waste Management Agency), Radioactive waste classification, website: https://international.andra.fr/radioactive-waste-france/waste-classification.

Journal Pre-proof

855 [35] K.-H. Schmidt, B. Jurado, C. Amouroux, C. Schmitt, *"General Description of*
856 *Fission Observables: GEF model code"*, Nucl. Data Sheets, vol. 131, 107-221
857 (2016).

Journal Pre-proof

Journal Pre-proof

Highlights

- Photofission is a promising technique to assay nuclear waste packages
- Photon activation analysis is used to characterize a 17.5 MeV Bremsstrahlung beam
- Photofission products cumulative yields have been determined for ^{239}Pu, ^{235}U and ^{238}U
- The contribution of neutron fission has been estimated with the MCNP code
- Photofission product yield difference makes actinides differentiation practicable

Journal Pre-proof

CRediT author statement:

M. Delarue: Methodology, Investigation, Software, Writing – Original Draft, Visualization, Formal analysis

E. Simon: Conceptualization, Methodology, Writing – Review & Editing

B. Pérot: Supervision, Writing – Review & Editing

P.G. Allinei: Software, Investigation, Resources

N. Estre: Investigation, Resources

E. Payan: Investigation, Resources

D. Eck: Investigation, Resources

I. Espagnon: Software

J. Collot: Supervision, Writing – Review & Editing

Journal Pre-proof

Declaration of interests

☒ The authors declare that they have no known competing financial interests or personal relationships that could have appeared to influence the work reported in this paper.

☐The authors declare the following financial interests/personal relationships which may be considered as potential competing interests:

Journal Pre-proof